





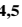

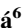




Understanding the Seismic Signature of Transtensional Opening in the Reykjanes Peninsula Rift Zone, SW Iceland



Special Collection:

Advances in understanding volcanic processes

Pınar Büyükkapınar^{1,2} , Marius Paul Isken^{1,2} , Sebastian Heimann² , Torsten Dahm^{1,2} , Daniela Kühn^{1,3} , Juliane Starke¹ , José Ángel López Comino^{4,5} , Simone Cesca¹ , Jana Doubravová⁶ , Egill Árni Gudnason⁷ , and Thorbjörg Ágústsdóttir⁷ 

¹German Research Centre for Geosciences (GFZ), Potsdam, Germany, ²Institute of Geosciences, University of Potsdam, Potsdam, Germany, ³NORSAR, Kjeller, Norway, ⁴Instituto Andaluz de Geofísica, Universidad de Granada, Granada, Spain, ⁵Departamento de Física Teórica y del Cosmos, Universidad de Granada, Granada, Spain, ⁶Institute of Geophysics, Czech Academy of Sciences, Prague, Czech Republic, ⁷Iceland GeoSurvey (ÍSOR), Kópavogur, Iceland

Key Points:

- Centroid moment tensors with $M_w > 2.7$ show strike-slip mechanisms and significant isotropic components, indicating complex interactions
- Magmatic intrusions form en-echelon dikes, inducing microearthquakes and triggering larger earthquakes at shallow depths
- Transtensional opening at the plate boundary is driven by dike intrusions, contributing to complex faulting and co-seismic volume expansion

Supporting Information:

Supporting Information may be found in the online version of this article.

Correspondence to:

P. Büyükkapınar,
pinar@gfz-potsdam.de

Citation:

Büyükkapınar, P., Isken, M. P., Heimann, S., Dahm, T., Kühn, D., Starke, J., et al. (2025). Understanding the seismic signature of transtensional opening in the Reykjanes Peninsula Rift Zone, SW Iceland. *Journal of Geophysical Research: Solid Earth*, 130, e2024JB029566. <https://doi.org/10.1029/2024JB029566>

Received 23 MAY 2024

Accepted 15 DEC 2024

Author Contributions:

Conceptualization: Pınar Büyükkapınar, Torsten Dahm

Data curation: Marius Paul Isken, Jana Doubravová, Egill Árni Gudnason, Thorbjörg Ágústsdóttir

Formal analysis: Pınar Büyükkapınar, Marius Paul Isken, Juliane Starke, José Ángel López Comino

Funding acquisition: Pınar Büyükkapınar

Abstract We analyze seismicity and centroid moment tensors (CMTs) on the Reykjanes Peninsula, Iceland, during the early phase of a widespread unrest period that led to multiple fissure eruptions between 2021 and 2024. We use a dense temporary seismic array, together with fiber-optic distributed acoustic sensing data, and incorporate first-motion polarities into the CMT inversion to improve accuracy, generating a total of 300 robust CMT solutions for magnitudes $M_w > 2.5$, focusing on 83 reliable $M_w > 2.7$ earthquakes for interpretation. The CMTs predominantly exhibit shallow strike-slip faulting, with a few normal faulting events compatible with tectonic stress. Interestingly, significant positive isotropic components are resolved, contributing up to 15% of the moment release. We also develop a new high-resolution seismic catalog of 34,407 events and show that larger shallow earthquakes at the plate boundary are preceded by the slow upward migration of microearthquakes from below, suggesting that intruding magmatic fluids interact with the oblique plate boundary to trigger slow slip events. We interpret our results as the seismic response to transtensional motion at the plate boundary in the brittle upper crust under shear, in response to stress changes induced by the intrusion of pressurized fluids in the lower crust. The complex interaction of multiple subparallel dikes with the plate boundary fault contributes to a broader deformation band that accommodates both tectonic and magmatic stresses. While the location and magnitude of the CMTs correlate with reactivated surface fractures and faults, the locations of intense, deep microseismic swarms indicate the sites of future fissure eruptions.

Plain Language Summary Magma intrusions can affect the Earth's crust by producing surface deformation, perturbing stress conditions, and triggering seismicity. The combined study of microearthquake swarms and the source mechanism of larger earthquakes provides insights into the interactions between magmatic fluid intrusions and the surrounding rock, which are key to understanding magmatic processes. Strong, widespread, and persistent seismic activity occurs on the Reykjanes Peninsula, Iceland, prior to the Fagradalsfjall and Grindavík eruptions between 2021 and 2024. By taking advantage of the dense deployment of seismic stations and fiber-optic cables, we are able to accurately resolve the mechanism of larger earthquakes at the plate boundary. The larger, significant events all occur at shallow depths and contain atypical source parameters, suggesting that fracture opening processes accompany the typical shear faulting. We also derived a high-resolution catalog of over 34,407 microearthquakes spanning 10 months. The pattern of seismicity in this catalog suggests that the ascent of magmatic fluids from the lower crust influences both seismic and aseismic behavior in the upper crust, leading to shear and tensile motions along the plate boundary. The study provides new insights into how transtensional opening mechanisms occur at plate boundaries.

1. Introduction

The Reykjanes Peninsula (RP) in southwestern Iceland represents a transtensional plate boundary between two offset spreading axes of a mid-ocean ridge system, influenced by seismicity, deformation, geothermal activity, and volcanism (Figure 1). The north-trending mid-Atlantic ridge emerges from the ocean at the southwestern corner of the RP, turning into a 60-km-long N70° – 75°E-trending plate boundary, highly oblique to the spreading direction of N(121 ± 3)°E (Keiding et al., 2009). The minimum compressive stress S_{hmin} from microearthquakes indicates an average of N(120 ± 6)°E. Kinematic plate boundary models based on GNSS indicate a 18 ± 2 mm/yr left-lateral motion and 7 ± 1 mm/yr opening along the central part of the plate boundary

© 2024. The Author(s).

This is an open access article under the terms of the [Creative Commons Attribution License](https://creativecommons.org/licenses/by/4.0/), which permits use, distribution and reproduction in any medium, provided the original work is properly cited.

Investigation: Pınar Büyükkapınar, Marius Paul Isken, Torsten Dahm, Juliane Starke, José Ángel López Comino
Methodology: Pınar Büyükkapınar, Marius Paul Isken, Sebastian Heimann, Daniela Kühn
Software: Pınar Büyükkapınar, Marius Paul Isken, Sebastian Heimann, Daniela Kühn
Validation: Pınar Büyükkapınar, Marius Paul Isken
Visualization: Pınar Büyükkapınar, Marius Paul Isken, Torsten Dahm
Writing – original draft: Pınar Büyükkapınar
Writing – review & editing: Pınar Büyükkapınar, Sebastian Heimann, Torsten Dahm, Daniela Kühn, Simone Cesca, Egill Árni Gudnason, Thorbjörg Ágústsdóttir

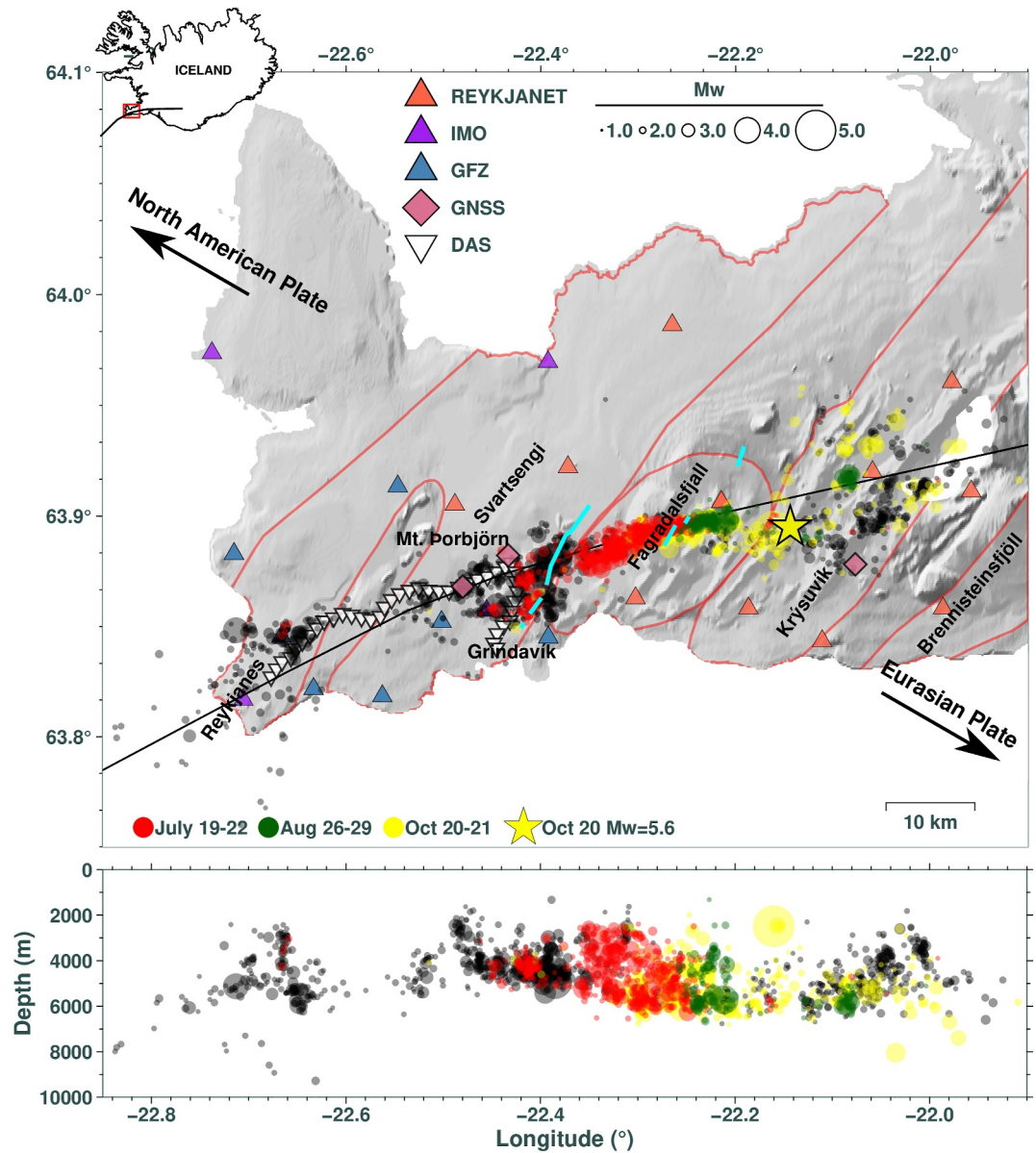


Figure 1. Seismicity and distribution of seismic stations in the study area in 2020. The red rectangle and black line in the inset figure show our study area and the plate boundary axis on the RP (Sigmundsson et al., 2022). Triangles show the locations of broadband seismic stations; orange, purple, and blue colors indicate the seismic networks of Academy of Sciences of the Czech Republic (REYKJANET), Icelandic Meteorological Office (IMO), and MAGma-GEOFON (German GeoForschungsZentrum, GFZ), respectively. Pink diamonds indicate the GNSS stations operated by IMO, and white inverted triangles show the 40 virtual (selected) channels on the fiber-optic cable operated by GFZ (MAGIC). The colored circles show the seismicity in 2020 for depth. Three swarm periods are highlighted (July 19–22, red; August 26–29, green; October 20–21, yellow). The yellow star indicates the location of the 20 October 2020, $M_w = 5.6$ event at Krýsuvík. The cyan lines show the eruptive fissures active from 2021 to 2024. The areas within the red lines show the volcanic systems of Reykjanes, Svartsengi, Fagradalsfjall, Krýsuvík, and Brennisteinsfjöll from west to east, respectively (Sæmundsson & Sigurgeirsson, 2013). The arrows show the direction of the full 19–20 mm/a spreading across the RP between North America and Eurasia.

on the RP (Keiding et al., 2009). The predicted average S_{hmin} from this model trends $N(132 \pm 1)^\circ E$ and would favor rupture on N-S right-lateral and NE-SW left-lateral conjugate faults, if a friction coefficient of 0.6 is assumed.

The oblique plate boundary manifests as a 5– to 10–km–wide wide seismic zone and a series of volcanic systems, including Reykjanes, Svartsengi, Fagradalsfjall, Krýsuvík, Brennisteinsfjöll, and Hengill (see Figure 1; Sæmundsson & Sigurgeirsson, 2013), accompanied by high-temperature geothermal fields (Flóvenz et al., 2022). These volcanic systems are arranged in an en-echelon pattern relative to the plate boundary (Clifton & Kattenhorn, 2006; Einarsson, 2008) and comprise eruptive fissures, tectonic faults, and fractures created during repeated basaltic eruptive phases. Over the last 4,000 years, historical volcanism has been episodic, with rifting and volcanic episodes lasting 400–600 years, interspersed with periods of dormancy lasting 600–800 years (Sæmundsson et al., 2020; Sæmundsson & Sigurgeirsson, 2013).

Intense earthquake swarms frequently occur on the RP (Björnsson et al., 2020; Einarsson et al., 2020; Klein et al., 1977), where the transcurrent motion of the plate boundary is accommodated by either left-lateral motion along the plate boundary or by right-lateral motion on N-S striking rupture planes of earthquakes with magnitudes up to M 6 (Árnadóttir et al., 2004; Einarsson et al., 2023; Keiding et al., 2009) at depths between 2 and 6/7 km (Einarsson, 1991). The latest cycle of seismic unrest began in late 2019 in the area of Þorbjörn-Svartsengi, characterized by cycles of local surface uplift and subsidence with rates of 3–4 mm/day (Cubuk-Sabuncu et al., 2021; Flóvenz et al., 2022). Seismicity intensified in early 2020, particularly in the Fagradalsfjall volcanic system, indicating active deformation and unrest linked to magma inflation and the ascent of magma through the upper crust. Initially, the focus was placed on the Svartsengi volcanic system due to shallow seismicity suggesting stress build-up from deep magma intrusion; however, the first volcanic eruption occurred more than 10 km east of Svartsengi.

On 19 March 2021, a first fissure eruption occurred in the Fagradalsfjall volcanic system near Geldingadalir (Figure 1), releasing 150 Mm³ of lava over six months and covering an area of 5 km² (Pedersen et al., 2022). Seismic activity before to this eruption had intensified in 2020, indicating the climax of magmatic processes at depth. Two further eruptions occurred in the same region on 3 August 2022 and 11 July 2023, a few kilometers northeast of the 2021 Fagradalsfjall eruption (e.g., Fischer et al., 2023). In late 2023 and early 2024, volcanic activity shifted west of Svartsengi, with fissure eruptions taking place at Sundhnúkar near Grindavík. These ongoing eruptions and seismic activity suggest that the RP remains in a phase of tectonic and magmatic unrest.

Recent advancements in monitoring techniques, such as TerraSAR-X interferometry, have documented widespread fault and surface fracture movements during the volcano-tectonic unrest on the RP between 2019 and 2021 (Ducrocq et al., 2024). Movements occurred both within the active plate boundary segment and to the north, primarily in the Svartsengi volcanic system and in Grindavík, which experienced the 2023 and 2024 fissure eruptions. While the movements at the Fagradalsfjall eruption site were smaller than in surrounding areas, surface fracture movements occurred in regions without major earthquakes, indicating long-term stress build-up. These observations provide crucial insights into understanding both near-surface tectonic strain and deeper magmatic processes.

A key question arising from this ongoing unrest is why relative opening and shear plate motion in the RP is accommodated by en-echelon fault systems and differently oriented crack modes, and whether co-seismic opening is observed. Factors such as plate boundary flexure, lithospheric structure, and rheology are likely critical. The upper crust of the RP, estimated to be 3–5 km thick and composed of basaltic extrusives, overlies the lower crust and Moho at approximately 15 km depth (Jenkins, 2024; Weir et al., 2001). The brittle-ductile transition (BDT) is thought to occur at a 6–7 km depth but rises to between 3 and 5 km beneath high-temperature geothermal fields (Flóvenz et al., 2022), where temperatures are estimated to reach 600°C (Violay et al., 2012). These factors, along with the interaction of faulting and magmatic processes at different depths, are likely to explain the transtensional dynamics of the plate boundary and are key to predicting future volcanic and seismic hazards.

In 2020, an extensive network of seismic sensors (Figure 1) was installed to provide comprehensive data on the RP transtensional rifting episode and the associated seismicity and seismic swarms in the Svartsengi and Fagradalsfjall volcanic systems. Additionally, repeated gravity experiments and InSAR studies offered critical data on cyclic surface deformation (Flóvenz et al., 2022). These data sets have the potential to elucidate how magmatic fluid input, intrusions, and plate motion release shear and tensional stresses at different depths. Seismic swarms and microearthquake seismicity enable researchers to investigate how localized strain from ascending

magma interacts with tectonic forces along the plate boundary. A thorough understanding of these dynamics is essential for addressing potential future eruptions.

Volcano-tectonic (VT) earthquakes provide further evidence of the complex interactions between tectonic and magmatic systems. Centroid moment tensor (CMT) analysis, based on full waveform inversions, has been crucial for understanding these dynamics. CMT can be decomposed into isotropic (M_{iso}) and deviatoric tensors (M_{dev}), with the latter composed of double-couple (M_{dc}) terms and compensated linear vector dipole (M_{clvd}) terms (Jost & Herrman, 1989). Non-double-couple (*nonDC*) terms, represented by $M_{iso} + M_{clvd}$, often arise in VT earthquakes where magma-induced pressure and tensile opening play a role in faulting processes. These (*nonDC*) can also originate from non-planar faults or multi-subevent earthquakes on parallel fault planes. Some studies even indicate mixed-mode ruptures on shear-tensile cracks for RP, with co-seismic opening and closing mechanism in the same region along the transtensional rift zone, associated to normal and thrust faulting, respectively (Hrubcová et al., 2021). These microearthquake source mechanisms, however, have not yet been confirmed by independent studies. A key question for the study at the RP is whether and at what depth *nonDC* terms and co-seismic opening have occurred, how it works, and what role it plays in understanding transtensional plate motion.

This research thus aims to address key aspects of how the transtensional opening of the brittle part of a plate boundary is mechanically realized, to explore the interaction between ascending melt batches, slow slip events, and the seismicity at the BDT, and to examine the consequences of the interaction between sub-parallel intrusions at depth and shear faults above. Leveraging an extensive seismic data set, including full moment tensors, microseismic catalogs, and distributed acoustic sensing (DAS) deployed in 2020, we aim to understand how magma-tectonic interactions drive fault formation, stress accumulation, and seismicity. These insights are critical for forecasting future volcanic and seismic activity in the RP.

2. Data and Methods

2.1. Detection and Location of Seismicity

The RP was seismically highly active during 2020, with several intense swarm episodes. According to the catalog of the Icelandic Meteorological Office (IMO, 1992), approximately 19,534 events were detected within 10 months in the area from 21.8° to 22.85°W to 63.78° and 64.10°N (Figure 1). We analyzed seismic data acquired by three different seismic networks deployed on the RP - REYKJANET (7E; Horalek, 2013), GFZ - MAGIC (9H; Dahm et al., 2020) and the IMO Icelandic National Network (SIL; Icelandic Meteorological Office, 1992). The data set consists of 27 stations distributed across the RP, each with a different installation period (Figure 1, Figure S1 and Table S1 in Supporting Information S1).

The high signal-to-noise ratio (SNR) facilitated the reliable picking of P-wave onsets at most of the stations (Figure S2 in Supporting Information S1). The azimuthal coverage of each event is abundant, which is essential to obtain reliable earthquake locations and source parameters with low uncertainties. In addition to these stations, DAS strain-rate recordings from a 21-km-long fiber-optic cable (Figure 1) were included. We used a subset of 40 spatially stacked channels downsampled to 100 Hz. The DAS interrogator was operated by GFZ Potsdam as part of the MAGIC HART Rapid Response Action.

Flóvenz et al. (2022) integrated DAS data to study very low magnitude seismicity and identified up to approximately 40,000 events with $M > -1$ within 7 months (January 1 to 1 September 2020). The study shows a concentration of shallow earthquakes (less than 4 km deep) near the center of uplift in Svartsengi. Deeper seismic events were rare during the 244-days monitoring period. Although the waveform stacking approach used by Flóvenz et al. (2022) to detect and locate seismicity was promising and successful, the earthquake catalog had some shortcomings. First, magnitudes were not included in the analysis. Second, the static grid points used to search for centroids were relatively sparse, which did not allow for detailed analysis of the spatial distribution of the earthquakes or their spatiotemporal migration.

In this study, we derive an earthquake catalog using *Qseek*—an automatic and waveform-based earthquake detector and locator (Figure 1, Figures S3 and S4 in Supporting Information S1). *Qseek* combines seismic phase arrivals provided by neural network phase pickers and waveform stacking with an efficient adaptive octree search. The resolution of the search volume is iteratively refined toward the seismic source location, allowing for a fast and accurate search. Calculation of moment and local magnitude from peak ground motions is included (Dahm et al., 2024). Location accuracy is improved by incorporating station-specific corrections (SST) and source-

specific station terms (SSST) into the search. The method has been demonstrated and validated for several large seismic data sets in different regions and geological settings (Büyükakpınar, Isken, Dahm, et al., 2024; Büyükakpınar, Isken, Heimann, et al., 2024). Our seismic catalog was generated using the local velocity model reported by Hrubcová et al. (2021). A comparison of the IMO and *Qseek* locations is shown in the Figure S5 of Supporting Information S1. A comparison of the local M_L model from Greenfield et al. (2020) and the M_W scale from *Qseek* with the seismic moment derived from CMT employing *Grond* is demonstrated in the Figure S6 of Supporting Information S1.

2.2. Centroid Moment Tensor Inversion

2.2.1. Method

We apply CMT inversion to earthquakes larger than $M = 2.5$ that occurred in 2020 and were captured by our combined network (Figure 1). We use a joint waveform and polarity inversion method (Figures 2 and 3) to retrieve the CMTs of earthquakes on the RP. To quantify the uncertainties of the retrieved results, a combination of non-linear inversion and bootstrap technique is applied, as it is implemented in the open-source software *Grond* (Heimann et al., 2018). A small subset of the waveform fits and CMT solution are shown in Figure 2 for a selected event. The full online report of CMT results produced in this study can be found at the link <https://data.pyrocko.org/publications/grond-reports/2020-iceland-reykjanes/> and as a Table in Supporting Information S1.

We solve the inverse problem of determining a source model given a set of observations using a probabilistic optimization approach (Akbarbayram et al., 2022; Cesca et al., 2023; Jamalreyhani et al., 2021). It consists of repeatedly searching for the model that minimizes the misfit between observed and forward modeled data, each time using a different perturbation of the objective function used in the data fitting. The results of these optimizations form an ensemble of source models that all explain the observations satisfactorily well. From this ensemble, it is possible to determine the uncertainties of the source model parameters and also the possible trade-offs between them. We call this method Bayesian bootstrap optimization BABO and it is explained in Dahm et al. (2018) and Kühn et al. (2020). It is based on the concept of Rubin (1981), who showed that, with a certain choice of weights, the resulting ensemble of bootstrap solutions can be treated as a non-parametric posterior distribution.

The source model parameterization consists of the location, depth, and time of the point-like earthquake origin (centroid) and of the six independent components of the moment tensor. Optionally a source duration can be added to the inversion parameters.

The forward modeling of synthetic waveforms uses an approach based on precalculated Green's functions (GFs; Heimann et al., 2019). We use the QSEIS code of Wang (1999) to compute the GFs. It uses the orthonormal propagator method to solve the wave equation for a layered viscoelastic half-space model. For the forward modeling of seismic phase onset polarities and travel times, we use the *Cake* tool, which is part of the *Pyrocko* software suite (Heimann et al., 2017).

The optimization is based on minimizing the misfit between observed and synthetic data. Following Kühn et al. (2020), we design the objective function to be minimized using an L1 norm as

$$M = \frac{\sum_i |w_i m_i|}{\sum_i |w_i n_i|}, \quad (1)$$

where m_i is the misfit for a specific recorded seismic waveform or phase attribute, n_i is a corresponding normalization factor, and w_i is a weighting factor. For seismic waveforms, the m_i and n_i are defined as (not showing the index i)

$$m = \sum_j |o_j - s_j| \quad \text{and} \quad n = \sum_j |o_j|, \quad (2)$$

where o_j and s_j are observed and synthetic samples, respectively. The samples are taken from filtered and tapered displacement waveform snippets or amplitude spectra. For seismic phase polarity records, we use

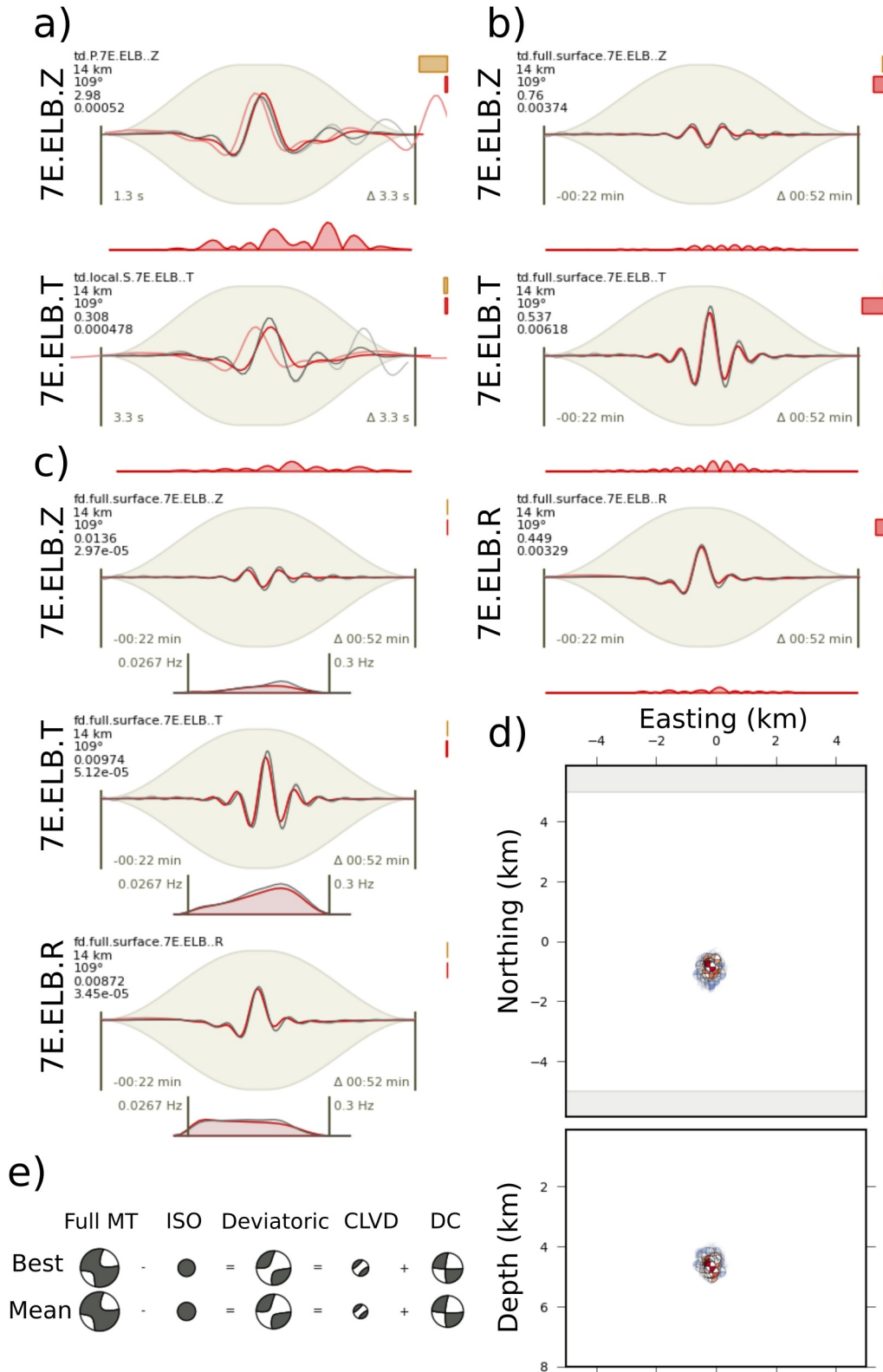


Figure 2.

$$m = \frac{1}{2}|o - s| \quad \text{and} \quad n = 1, \quad (3)$$

where o and s are the observed and synthetic polarities $\{+1, -1\}$.

Also following Equation 4 in Kühn et al. (2020), the weights w_i in (1) are composed as

$$w_i = w_{\text{balance},i} w_{\text{manual},i} w_{\text{bootstrap},i} \quad (4)$$

where the $w_{\text{balance},i}$ balance the contribution due to expected signal amplitude, depending on source-receiver distance, phase type, and applied signal processing; the $w_{\text{manual},i}$ can be used subjectively, and $w_{\text{bootstrap},i}$ are assigned by the BABO algorithm to perturb the objective function, a requirement for the bootstrap technique which is used to obtain uncertainties. Details are described in Kühn et al. (2020).

2.2.2. Data

We analyzed CMT for 300 events with magnitudes $M > 2.5$ using permanent and temporary seismic stations (27 stations in total) as well as DAS data measured along a 21 km long fiber optic cable running across the center of the seismic swarms (Figure 1). Full waveforms consisting of body and surface waves at broadband seismic stations, and first motion polarities are jointly inverted to resolve a full moment tensor. Seismic data quality assessments were performed visually. About 7,000 P-wave arrivals were manually identified and picked. The frequency ranges of 0.7–2.0 Hz and 0.04–0.2 Hz (hereafter referred to F1) were selected for body and surface waves, respectively.

2.2.3. Application and Parameters

Synthetic seismograms are calculated based on the local velocity model reported by Hrubcová et al. (2021) for a 250 m grid spacing from 1 to 50 km source-receiver distance and 0.1–10 km source depth for a sampling rate of 25 Hz. Theoretical arrival times for S-wave and surface waves were calculated using Cake software (<https://pyrocko.org/docs/current/apps/cake/index.html>).

Waveforms (Figure 2) and polarities (Figure 3) are combined to provide more detailed information about the source process (Alvizuri et al., 2018). While the surface waves were inverted in the time and frequency domains using the R, T, and Z components for the full waveforms, the body waves were inverted in the time domain using the T and Z components in time windows ranging from 0.1 s before to 0.3 s after the P and S arrivals, respectively. This setup was chosen as a result of sensitivity analysis, testing the stability of the result in terms of waveform fits when using different phases, amplitudes, and input data types. Synthetic traces are allowed to be shifted by up to ± 0.2 s relative to observed data. Balancing weights are applied to ensure an optimal weighting of different phases and distances (Heimann, 2011). In addition, manual weights were defined for each input data type (Kühn et al., 2020) giving more weight to the waveforms since they carry more reliable information on the source (Table 1). For the first motions, take-off angles were computed using the same velocity model as for the waveform GFs database. The parameters used in the CMT inversion are summarized in Table 1.

We applied 200,000 iterations in the inversion. The inversion provides the best and mean solutions besides source parameter uncertainties. Finally, 83 earthquakes ($M_w > 2.7$) out of 300 (Figures 4 and 5) were selected for a

Figure 2. Small subset of the Grond report for the 2020–07–20 (UTC) 08:15:12 $M_w = 3.3$ earthquake. Waveform fits for station 7E.ELB for (a) vertical (Z) and transverse (T) waveforms of the body waves in the time domain, (b) Z, T, and radial (R) waveforms of the surface waves in the frequency domain, and (c) the time domain, respectively. Information (left side, from top to bottom) gives station name with the component, distance to the source, azimuth of the station with respect to source, target weight, target misfit, and start time of the waveform relative to the origin time. The background gray area demonstrates the applied taper function. The bottom panel shows sample-wise residuals in time domain (red-filled), and amplitude spectra of observed and synthetic traces (gray and red-filled, respectively). Colored boxes to the upper right show the relative weight of the target during optimization within the entire data set (top box, orange) and the relative misfit contribution to the global misfit (bottom box, red). (d) Location of the ensemble of best solutions. Symbols show the best double-couple mechanisms, and colors indicate low (red) and high (blue) misfits. (e) Ensemble best and mean solutions decomposed into M_{iso} , M_{dev} , M_{clvd} , and M_{dc} parts. Symbol size indicates relative strength of the components.

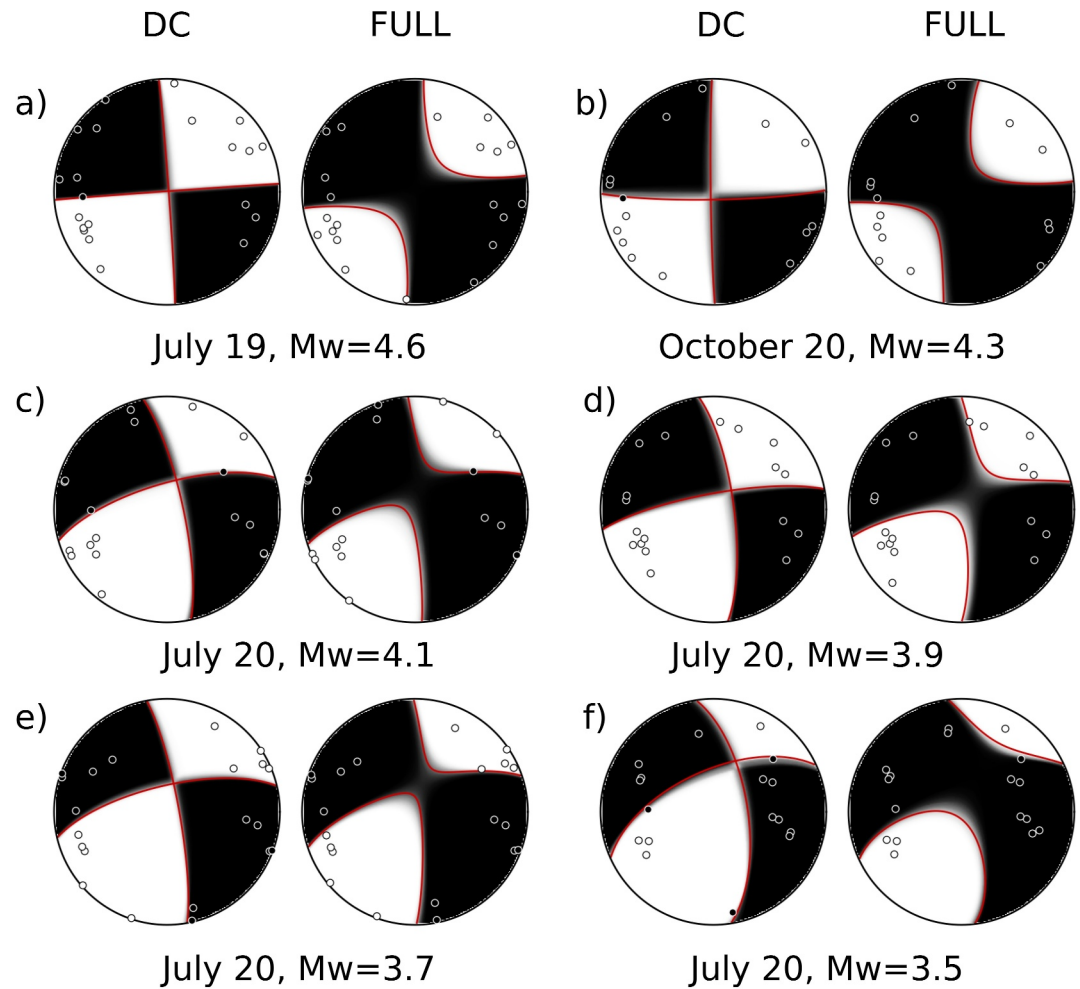


Figure 3. Lower-hemisphere projection of the P-wave radiation pattern of the full moment tensor (FULL) and the double-couple (DC) along with the first motion polarities for six selected earthquakes in 2020 a) 2020-07-19T23:36:13, M_w 4.6, (b) 2020-10-20T15:32:46, M_w 4.3, (c) 2020-07-20T06:23:00, M_w 4.1, (d) 2020-07-20T00:08:19, M_w 3.9, (e) 2020-07-20T07:09:13.16, M_w 3.7, (f) 2020-07-20T08:20:30, M_w 3.5. The black circles with white outlines and white circles with black outlines demonstrate the upward and downward motion of the first polarities, respectively.

common interpretation based on the robust centroid locations, convergence of model parameters, low misfit, and sufficient azimuthal coverage (Figure 4). The full reports of waveform fits for all 83 events are provided in the link repository as interactive web reports (see Open Research). They include the waveform and station distribution assessments, waveform and spectral fits of the best and ensemble models, information on the convergence and statistics of the optimization, and the evaluation of the contribution of the individual input data, and model parameters uncertainties, including centroid locations and CMT components.

3. Results

3.1. Event Locations

The high-resolution earthquake catalog derived by *Qseek* with the applied SSST corrections is shown in Figure 1. The catalog consists of 34,407 locations for the period from January 1 through 31 October 2020 (Figure S5 in Supporting Information S1). Flóvenz et al. (2022) detected slightly more events with the predecessor method of *Qseek* (*Lassie*) including additional DAS data. However, we omitted the DAS data here because the neural phase picker is not trained on DAS data. The earthquake hypocenters in the IMO catalog were determined manually using the single-event location method, with approximately 15,000 coinciding with those in the *Qseek* catalog. However, *Qseek* earthquake locations are more clustered and events are better aligned on 2D structures that can be

Table 1
Parameters Used in CMT Inversion

No.	Data	Inversion domain	Component(s)	Frequency band [Hz]	Time window	Weight
1	Full waveform	Time Domain	Radial, Transverse, Vertical	$f_{\min} : 0.04$ $f_{\max} : 0.2$	$t_{\min} : \text{begin}$ $t_{\max} : \text{end}$	0.5
2	Full waveform	Frequency domain	Radial, Transverse, Vertical	$f_{\min} : 0.04$ $f_{\max} : 0.2$	$t_{\min} : \text{begin}$ $t_{\max} : \text{end}$	0.5
3	P-wave	Time Domain	Vertical	$f_{\min} : 0.7$ $f_{\max} : 2.0$	$t_{\min} : t_P - 0.1 \text{ s}$ $t_{\max} : t_P + 0.3 \text{ s}$	1.0
4	S-wave	Time Domain	Transverse	$f_{\min} : 0.7$ $f_{\max} : 2.0$	$t_{\min} : t_S - 0.1 \text{ s}$ $t_{\max} : t_S + 0.3 \text{ s}$	0.5
5	P-wave	Arrival time	Strain Rate (DAS)	-	-	0.25
6 ^a	First motions	Polarity	Vertical (Z)	-	-	0.1

Note. No. Represents the number of each target group. Data indicates which type of record is inverted. The inversion domain indicates the normalization family. f_{\min} and f_{\max} are minimum and maximum frequency (Hz) used to pre-filter data before inversion. Time windows given by “begin” and “end” represent the full waveform for each event and t_P and t_S for the P and S-wave arrival time. The weight shows the relative contribution to the objective function for each target group. ^aFirst motions are inverted only for selected events (see Figure 3).

interpreted as faults or fissures. The number of isolated deep events is smaller in the new *Qseek* catalog, which has a narrower depth range. The mean depth of all events is slightly greater in the new *Qseek* catalog compared to the previous *Lassie* catalog (Flóvenz et al., 2022), which may be explained by the inclusion of DAS data in the latter, which allowed for the detection of local, shallow microearthquakes situated below the fiber cable.

3.2. Centroid Moment Tensors

Figure 4 shows the statistics of the decomposed source parameters. Our results indicate positive M_{iso} components (Figure 4a) around $14.5 \pm 4.9\%$. In contrast, M_{clvd} components fluctuate around zero, ranging between -50% and 60% , with a mean of $6.9 \pm 12.9\%$ (Figure 4b). No significant correlation ($R = -0.02$) is observed between the two *nonDC* components (Figure 4c). The centroid depths of the events are mostly located in the shallow 4 km, with a mean value of 3.0 km (Figure 4d) and a depth uncertainty of 0.2 km (Figure 4e). We also compared the *nonDC* components with centroid depths (Figures 4f and 4g) and magnitudes (Figures 4h and 4i). Larger magnitude events tend to have lower M_{clvd} components, likely due to improved SNR. In contrast, M_{iso} shows a slight increase as centroid depth increases. No temporal variation is recognizable in either of the components (Figure S7 in Supporting Information S1). The complete list of CMT inversion parameters and their uncertainties is provided in Supporting Information S2 and visualized in Figures 4 and 5. Different analyses show that the source parameters remain stable. We varied the selection of stations, phases, data types, frequency ranges, and performed inversions using different velocity models. The CMTs remain consistent across these tests, irrespective of the velocity models and frequency bands used (see Supporting Information S1, Figures S8 and S9).

Figure 5 depicts the Hudson plot for the *nonDC* source components (Hudson et al., 1989). The origin of the Hudson plot represents a source with a pure double-couple moment tensor ($DC = 100\%$). Crack opening is located in the upper-left near the positive dipole and the crack closing is in the lower-right near the negative dipole. Pure explosions and implosions emerge on the vertical axis of the diagram, +Isotropic and -Isotropic, respectively. The solutions consistently cluster in the upper half of the Hudson plot, indicating that a positive M_{iso} component is prominent. On the contrary, the scatter for the horizontal axes is symmetric, indicating that a non-zero M_{clvd} component is not resolved.

Figure 6 shows well-resolved CMTs. They represent predominantly strike-slip earthquakes on either EW (left-lateral) or NS (right-lateral) rupture planes. The centroid locations derived from moment tensor inversion align in the N70°E direction along the plate boundary on a segment within ± 15 km of the 2021 eruption site (Figure 6). The average centroid location uncertainties are ± 0.3 km (N) and ± 0.2 km (E), respectively. We do not observe a systematic change in the orientation of the DC component in the region near Svartsengi, which experienced strong uplift-subsidence cycles in 2020.

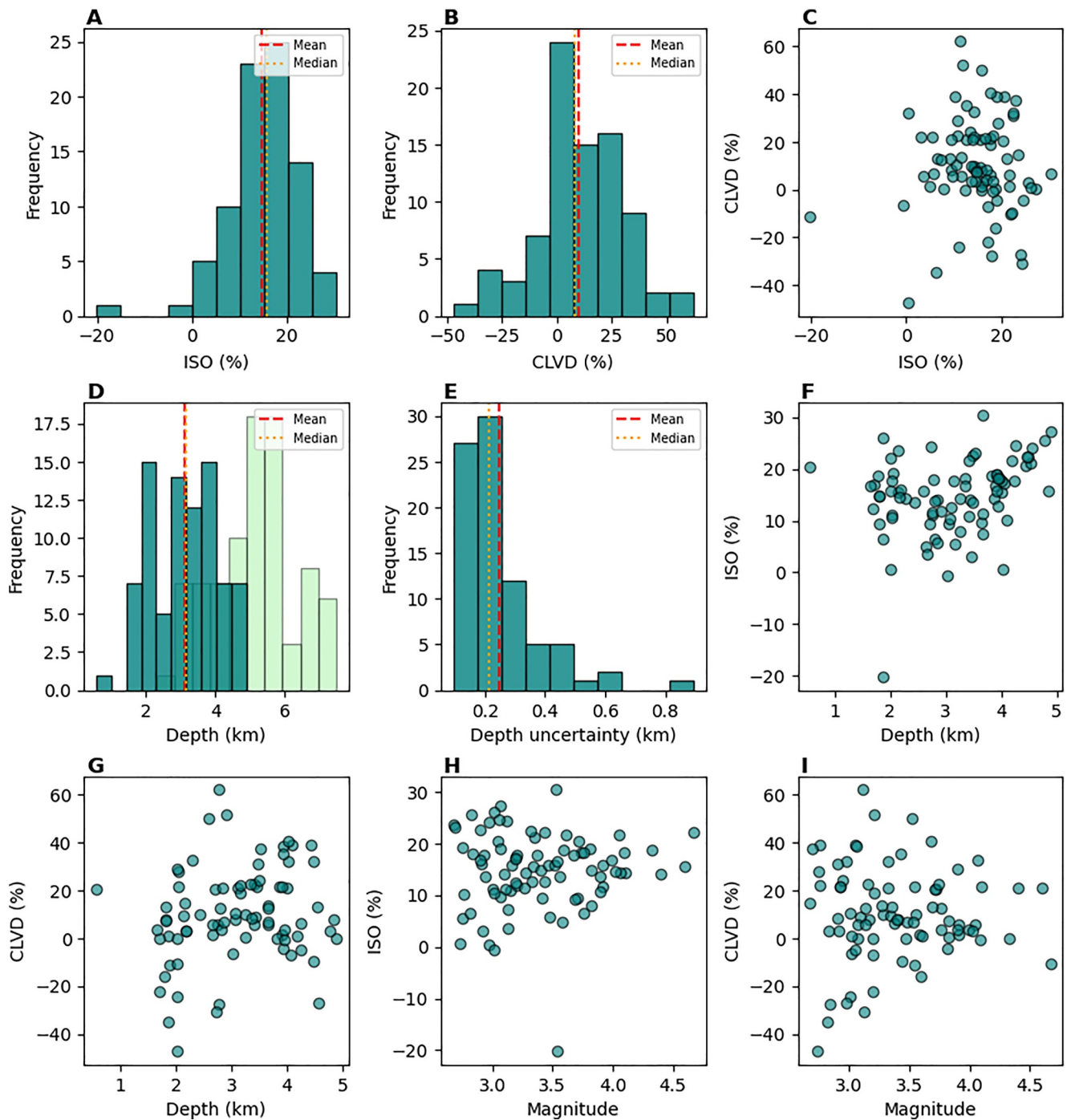


Figure 4. The full CMT decomposition results are shown in dark green. The red dashed lines represent the mean, while the orange lines show the median values. Histograms of (a) M_{iso} and (b) M_{clvd} (for definitions see e.g., Dahm & Krüger, 2014); (c) M_{clvd} vs. M_{iso} ; histograms of (d) centroid depths compared to hypocentral depths reported by IMO (light green color) and (e) depth uncertainty. Centroid depth (f), (g) and magnitude (h), (i) versus M_{iso} and M_{clvd} components, respectively.

Several sensitivity analyses were applied to the data set to understand the reliability of our results, because in the case of earthquakes with significant *nonDC* components, the magnitude of M_{dc} and M_{iso} components can vary significantly for small perturbations of the inversion parameters (Templeton & Dreger, 2006; Zahradnik et al., 2008). To evaluate the dependence of the results on the velocity model, we inverted the events employing three additional velocity models (Model 2, Model 3, Model 4) in Figure S8 of Supporting Information S1 derived from Hrubcová et al., 2021; Stefánsson et al., 1993; Tryggvason et al., 2002). GFs were generated with the same

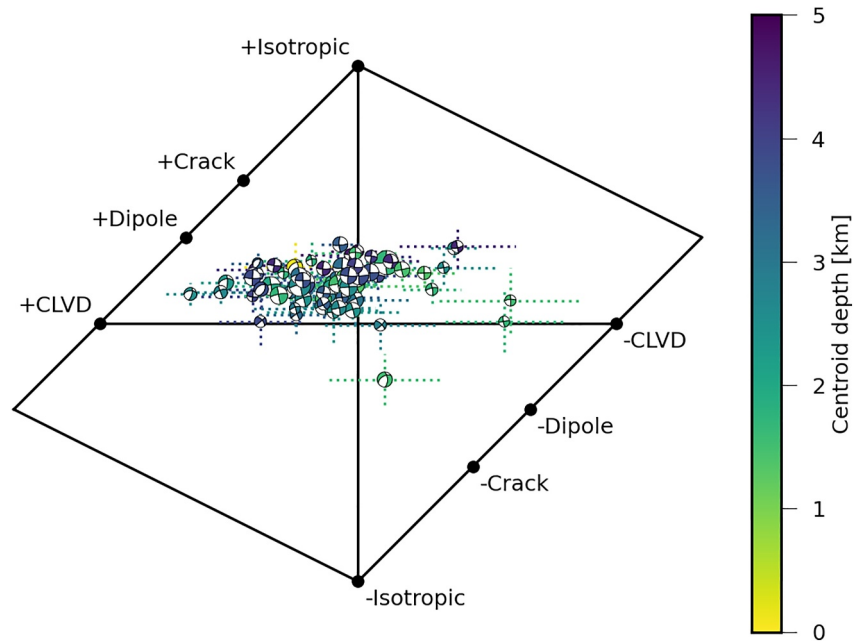


Figure 5. Non-Double Couple components of all CMT inversion results in the Hudson diagram. The beach-balls depicting double-couple part of the mean CMT solutions of all bootstrap-chains, colored by centroid depth. Dotted lines indicate the uncertainties in the M_{iso} and M_{cld} components.

parameters for all models. For Model 2, a shallow low-velocity layer was added to Model 1 to see the effect of near-surface properties on the inversion. The M_{iso} components are estimated to be $14.6 \pm 4.6\%$, $15.8 \pm 5.2\%$, and $15.7 \pm 5.2\%$ for the Model 2, Model 3, and Model 4, respectively, while the M_{cld} components are estimated to be $7.6 \pm 12.3\%$, $6.0 \pm 12.6\%$, and $6.0 \pm 12.7\%$. The mean centroid depths are 3.1 ± 0.2 km, 2.8 ± 0.2 km, and $2.8 \pm$

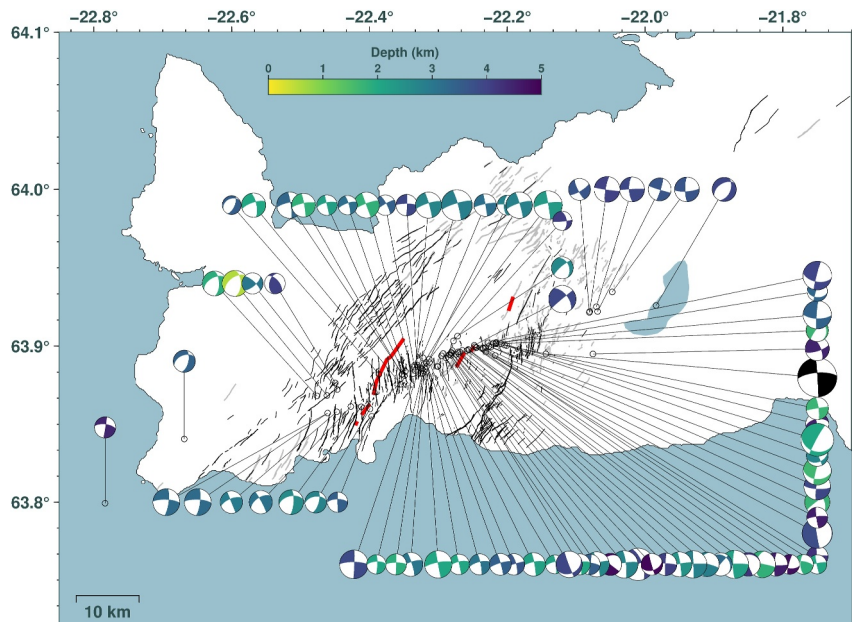


Figure 6. The beach-balls depicting double-couple part of the CMT solutions (lower hemispheric projections) of 83 selected earthquakes ($M_W > 2.7$) retrieved in this study. The colors of the beach-balls indicate the centroid depths of the earthquakes. The black beach-ball indicates the CMT of the 20 October 2020 $M_W = 5.6$ event at Krýsuvík (GEOFON). Gray and black lines indicate surface fissures and faults that were active in 2019 and 2020–2021, respectively (Ducrocq et al., 2024). Red lines indicate eruptive fissures active from 2021 to 2024.

0.2 km for the three different velocity models (Figure S8 in Supporting Information S1). In summary, the sensitivity analysis confirmed the presence of positive *M_{iso}* components around 10%–20%, shallow centroid depths, and nearly zero *M_{clvd}* components on average.

The frequency band used in the CMT inversion can also affect the results and interpretation. For this reason, we evaluated the CMT inversion results obtained with three additional different frequency bands depending on the source–receiver distance, F2: 0.7–2.0 Hz and 0.1–0.2 Hz for body and surface waves, respectively, F3: 1.0–2.5 Hz and 0.1–0.2 Hz, and F4: 1.0–2.5 Hz and 0.05–0.15 Hz (Figure S9 in Supporting Information S1). The means of the *nonDC* components are estimated as follows: $M_{iso} = 14.7 \pm 4.5\%$ and $M_{clvd} = 8.0 \pm 11.8\%$ for F2, $M_{iso} = 14.1 \pm 4.7\%$ and $M_{clvd} = 8.4 \pm 12.5\%$ for F3, and $M_{iso} = 15.7 \pm 4.4\%$ and $M_{clvd} = 5.6 \pm 13.2\%$ for F4, respectively. The means of centroid depths are 3.1 ± 0.2 km, 3.0 ± 0.3 km, and 3.2 ± 0.2 km for the three different filter ranges, respectively (Figure S9 in Supporting Information S1). We observe no discernible dependence of the parameters on the frequency bands, increasing the confidence in the accuracy and reliability of our results.

Furthermore, inversion results for small magnitude events ($M < 4.0$) can be affected by ambient noise. For example, in Iceland, the microseism noise from oceanic waves during storms can dominate the signals in the 0.04–0.2 Hz frequency range, which was used for surface wave inversion. Such unwanted noise can lead to artificial *nonDC* components. To understand the impact of microseisms caused by oceanic waves, we first invert all earthquakes with magnitudes larger than 2.5 (300 events). Subsequently, we inverted microseism signals contaminated by noise in the frequency band of 0.04–0.2 Hz. For both analyses, the mean of the distribution of *nonDC* components is zero, thus demonstrating that moment tensor solutions are not systematically biased by noise in this frequency band, and the volumetric components found during the inversion of the events are reliable (see Figure S10 in Supporting Information S1).

Events are clustered in both time and space. For example, major earthquake sequences occurred in July, August, and October 2020, represented by red, green, and yellow in Figure 7. Figure 7a shows the dominant mechanisms and the distribution of the CMTs in a triangular diagram. Pressure, tension, and null axes (P, T, and B axes, respectively) are indicated in Figure 7b. The P axes display a NE–SW alignment, while the T axis is sub-horizontal with an azimuth of $\sim 130^\circ$, which roughly corresponds to the direction of the least principal stress on the RP (Keiding et al., 2009). In Figure 7c, we present the mean full moment tensor solutions of the clusters.

4. Discussion

4.1. Evolution of Seismicity Along Tectonic and Volcanic Structures

Figure 7c shows four selected profiles to discuss the spatiotemporal evolution of seismicity and the occurrence of larger magnitude earthquakes with possible future fissure eruptions. Profile p1 trends $E15^\circ N$ and lies along the oblique plate boundary. Profiles p2, p3, and p4 run along the Reykjanes, Svartsengi and Krýsuvík volcanic systems, respectively, and are oriented perpendicular to S_{lmin} , approximately aligning with the mean direction of the P-axes in Figure 7a. Thus, shear stresses are assumed to be low or negligible on profiles p2–p4, while they are significant along or perpendicular to profile p1. Earthquakes rupturing the plate boundary in p1 are assumed to release shear stress directly, while migrating seismicity along profiles p2–p4 is interpreted as being induced by hydraulic or magmatic fracture growth at depth.

A second measure for distinguishing between intrusion-induced and tectonic earthquakes is the rate of migration of seismic fronts and back-fronts. While most aftershocks are activated immediately or shortly after the occurrence of a major tectonic event and sample approximately the size of the rupture plane of the main shock, the migration of intrusion-induced earthquakes is much slower, in the range of a few hundred meters or kilometers per hour for magma dikes rising from depth (Dahm, 2000; Rivalta & Dahm, 2006) and about 10–15 km/hr for lateral propagating dikes near the surface (Einarsson & Brandsdóttir, 1980; Sigmundsson et al., 2024). In the following, we select time windows of a few days or weeks along the specific profiles (Figure 7d) and project the seismicity and CMTs along horizontal and vertical sections. Only a few sections are included in the main text, while more examples are provided in the Supporting Information S1. For each profile, a gif animation of the time-space evolution of the seismicity is provided as a Zenodo repository <https://doi.org/10.5281/zenodo.13882152>, as it would be difficult to present it with static figures.

Figure 8 shows the seismicity at p1 during the first quarter of 2020 until April 24 (day 114). During this period, only three CMTs with $M_w > 2.7$ were retrieved, often in the boundary region of a developing swarm, and all

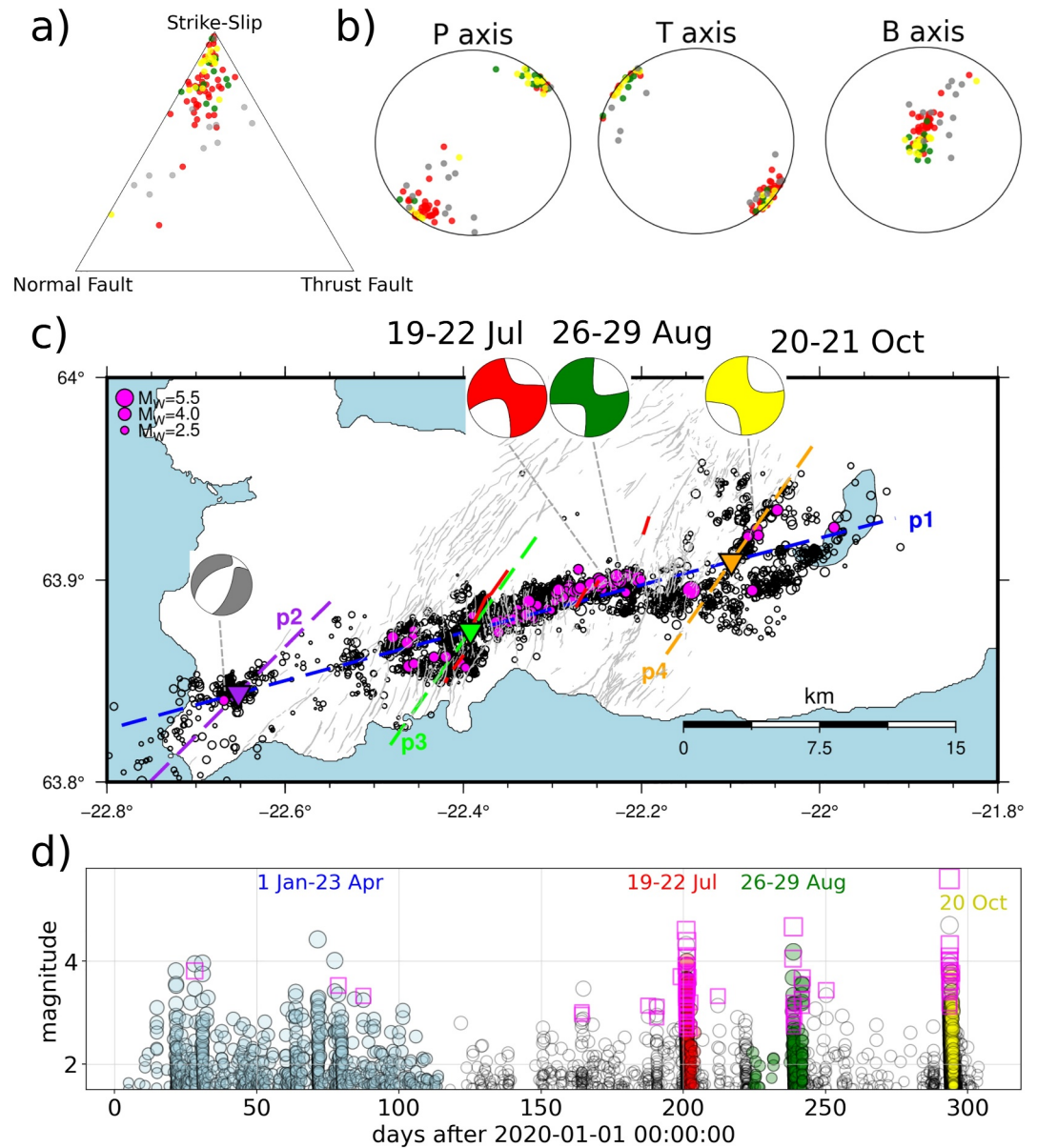


Figure 7. (a) The triangle diagram displays the distribution of strike-slip, normal, and thrust fault mechanisms, with circles representing the earthquakes. (b) P, T, and B axes of the earthquakes. (c) Selection of profiles p1 (blue), p2 (purple), p3 (light green), and p4 (orange), which run along the main plate boundary, Reykjanes, Svartsengi, and Krýsuvík volcanic systems, respectively. The crossing points of profiles p2-p4 with p1 are marked by inverted triangles. Earthquakes are indicated by black circles, while larger ones—83 events with CMTs of $M_W > 2.7$, retrieved in this study—are plotted in magenta. The composite full moment tensor solutions for activity during July 19–22 (red), August 26–29 (dark green), and October 20–21 (yellow), 2020, are provided. The red lines show the eruptive fissures active from 2021 to 2024, while gray lines indicate surface fissures and faults that were active from 2019 to 2021 (Ducrocq et al., 2024). (d) Time evolution of the seismic activity is illustrated to discuss the swarm phases, marked by color-filled circles in (c), with light blue indicating activity between January 1 and April 23. The remaining events are drawn in black, and larger events with CMTs are represented by magenta squares in the M_W over time plot.

occurring at depths of about 3.8 km. Interestingly, the first moderate microearthquake swarm started in the east beneath Krýsuvík at a profile length of 10 km (day 12) and 15 km (day 15). Subsequently, the swarm activity seems to jump westward (e.g., swarm at -2 km between Grindavík and Fagradalsfjall on day 22, at -7 km beneath Svartsengi on day 24 or at -15 km beneath Reykjanes on day 47). Over time, however, the seismic

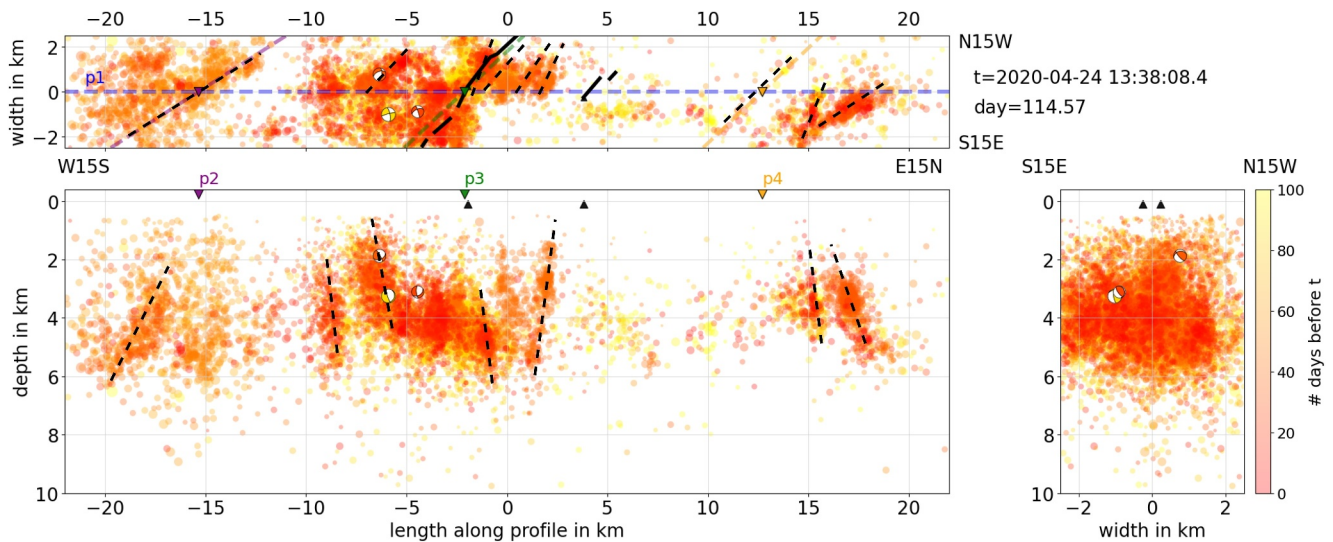


Figure 8. Profile p1 (blue dashed line), trends $E15^{\circ}N$ and lies along the oblique plate boundary, showing seismicity up to day 114 ($t = 2020-04-24\ 13:38:08.4$). The size of the circles represents M_W , while the color indicates the time of occurrence in days before the selected day (here, day 114). Earthquakes for which moment tensors were computed are indicated by beach-balls. Upper panel: p2 (purple), p3 (green), and p4 (orange) profiles are plotted and marked by inverted triangles where they cross p1. Thick black dashed lines and thinner black lines indicate volcanic fissure zones and elongated structures, based on interpretations from this study. Bottom panel: The crossing points of p2 (purple), p3 (light green), and p4 (orange) with p1 are marked again by inverted triangles at the top of the depth section. Black dashed lines show sub-vertical channels (dikes), as discussed in our study. Black triangles indicate where eruptive fissures at Fagradalsfjall (2021–2023) and Svartsengi (2023–2024) cross p1.

swarms occurred along the entire plate boundary, except for a segment between 3 and 13 km, where the first microearthquake swarms appear in our catalog.

The earthquakes often occur at depths between 1 km and 6–7 km. A very interesting observation from Figure 8 is that individual swarms during this time typically sample a large depth range, but have little lateral extent along the plate boundary so that they appear as sub-vertical channels of 3–4 km length in the vertical section of p1. In the map view (upper panel in Figure 8), they activate elongated structures of about 2–3 km in length that cross p1 and trend toward the volcanic fissure zones. These are typical dimensions and shapes of buoyancy-driven dikes (Dahm, 2000). The swarm activity is therefore interpreted as intrusive, sub-vertical fractures (dikes) crossing the plate boundary and fed by magmatic reservoirs below 7 km depth. For instance, the swarm that became active later on day 187.9, at a profile length of 15 km generated a M_W 3.1 normal faulting event at a depth of 3.4 ± 0.5 km (Figure S11, see also S15 in Supporting Information S1), with nodal planes striking in the direction of the p2 hydrofractures (e.g., Figure 7c).

We observe no clear correlations between GNSS deformation and larger earthquakes in a swarm, except for the M_W 5.6 earthquake on October 20. This earthquake produced co-seismic displacements on the horizontal components at the nearby GNSS station KRIV (see Figure S12 in Supporting Information S1). Apart from this example, GNSS stations were often many kilometers away from the moderate-sized earthquakes. The expected surface displacement from the deep and small-sized intrusions with only 2 km width and 3–4 km vertical length is very small, such that the GNSS apparently may not resolve an individual deep intrusion. For example, using a 2D boundary element method, we simulated a dike with a vertical length of 5 km and an overpressure of 1 MPa, with its upper tip located 6 km below the surface (half-space model, Young's modulus 50 GPa, Poisson ratio 0.25). This dike produces a maximum vertical and horizontal displacement of ± 3 mm and ± 1.5 mm at the surface, respectively, which is then distributed over a distance of more than 20 km. The displacement from a 3D dike simulation would be even smaller. Variations in daily and hourly GNSS station data are too large to resolve such small intrusions. However, the July 2020 swarm near the future eruption site at Fagradalsfjall may have triggered a trend change at the GPS stations SKSH and SENG, west and north of Mt. Þorbjörn, respectively (see Figure S12 in Supporting Information S1).

A notable observation is that these repeated "intrusion events" are widespread across the en-echelon structures. As we will see, this type of distributed intrusive activity continues throughout the analysis period in 2020, including at sites where fissure eruptions occurred in 2021, 2022, 2023, and 2024. If the massive intrusions at

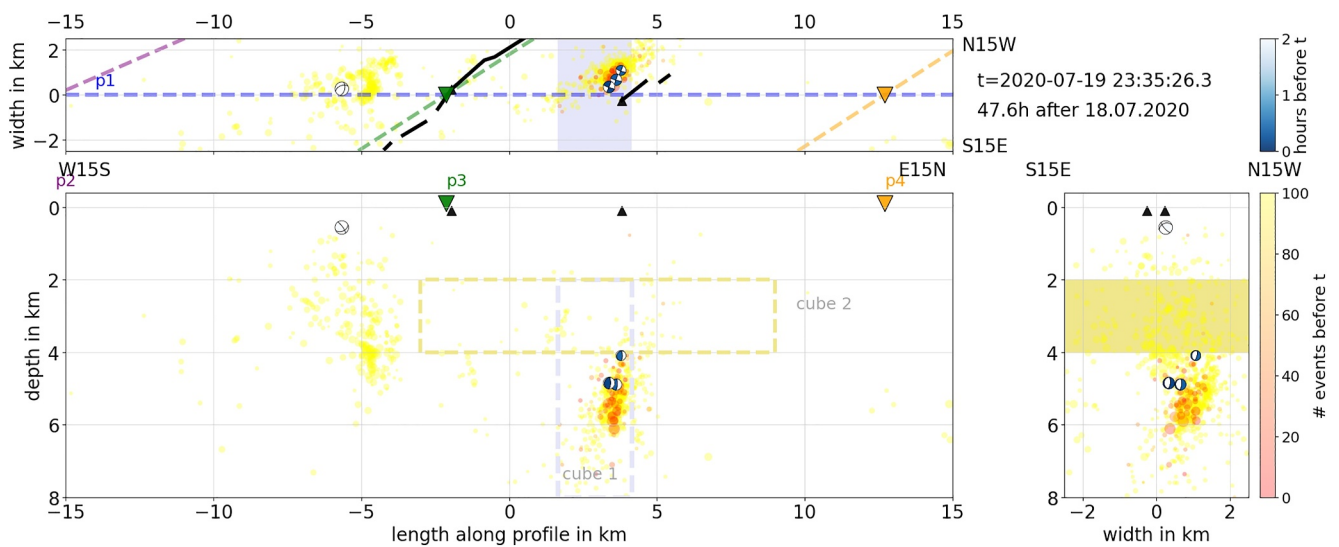


Figure 9. Snapshot of seismicity along profile p1 (blue dashed line) 47.6 hr after 18 July 2020. The color scale represents the number of events that occurred just before the given time (t). Two cube volumes are indicated by the gray and yellow areas with dashed lines, which define the volumes for the projection onto vertical and horizontal lines in Figure 11 based on our interpretation for further discussion. For an explanation of symbols, please see Figure 8.

depth are all related to magma migration, the system of sub-parallel magma dikes likely forms reservoirs (Kühn & Dahm, 2008) that are emptied by fissure eruptions. In addition, sill-type reservoirs may have formed.

In Figures 9 and 10, we unravel the details of a swarm's evolution, focusing on the example from July 19–22, 2020, when a significant number of stronger earthquakes were induced at the plate boundary, preceded by a deep, upward-migrating swarm. Two snapshots are shown just 2 hours apart. Unlike before, the colored circles show the number of events that occurred before the current time allowing the progression of activity to be resolved. Note that the shallowest earthquake for which a moment tensor could be resolved (M_w 3.7) occurred on July 18 (day 200) at a depth of only 558 ± 154 m (white circle at -6 km distance in Figure 9), just beneath the site of the future Svartsengi eruptive fissure, and is likely related to the swarm activity described here. In the first image (47.6 hr after July 18, 00:00), a vertical cluster of microearthquakes can be seen in cube volume 1, which is delineated based on our observational data of seismicity patterns similar to cube 2). This volume encompasses depths from approximately 4.5–6.5 km, highlighting areas where seismic activity is concentrated. In this phase, the calculated

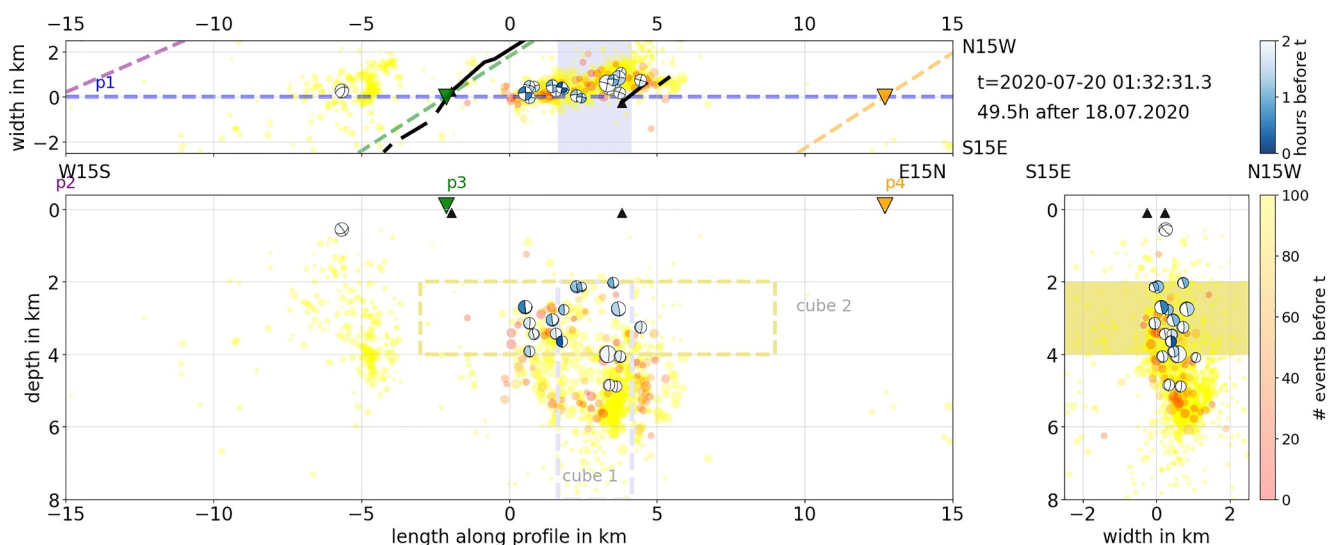


Figure 10. Same as Figure 9, but 2 hr later.

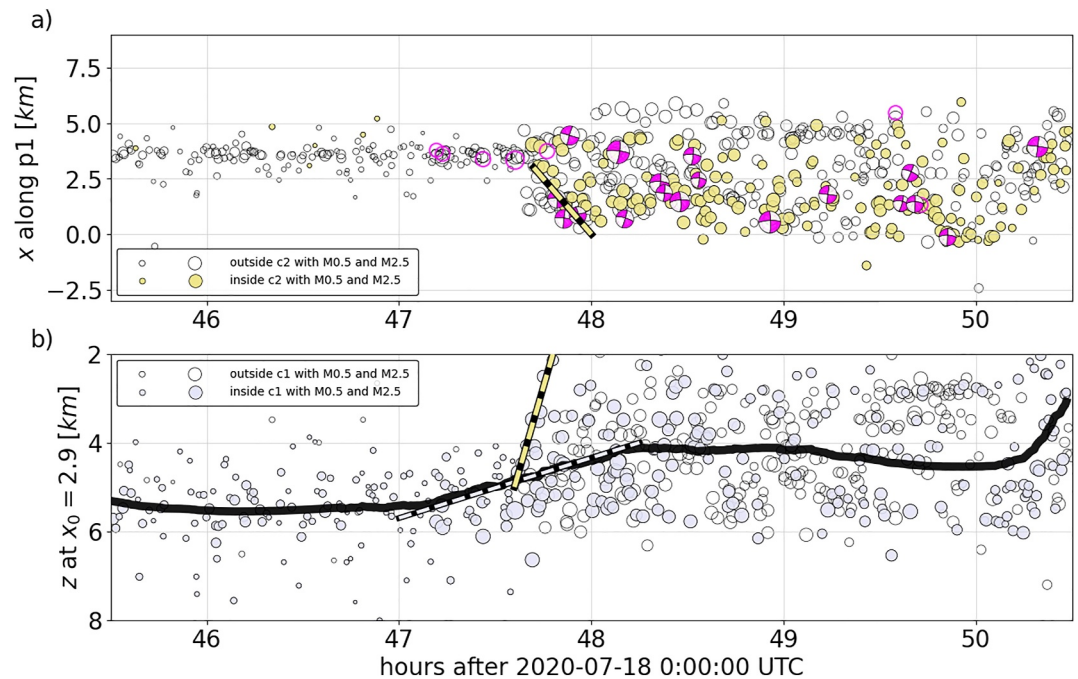


Figure 11. Deep intrusion phase between July 19 and 20, 2020. (a) Time-distance plots for earthquakes (circles) projected along profile p1 onto horizontal line at a depth of $z = 3$ km and (b) vertical line (at $(x, y) = (2.9, 0)$ km). The filled yellow and gray circles in (a) and (b) are events projected to the x and z axes from the cubes 2 and one indicated in Figures 9 and 10, respectively. The magenta beach-balls represent larger earthquakes ($M_w > 2.7$) for which CMTs could be calculated in this study. The gray-dashed and yellow-dashed lines indicate migration velocities of about 1.36 km/h and 10 – 15 km/h, respectively. The continuous black line in (b) shows the least squares filtered average of events inside cube 1 using a window length of 150 m and a polynomial order of 3.

b -value is higher than 1.5, indicating a relatively higher proportion of smaller earthquakes compared to larger ones (Figure S13 in Supporting Information S1). In map view, the events extend on a fracture structure that crosses the plate boundary profile p1 with a trend of $E35^\circ N$. A few minutes before the snapshot time, three larger earthquakes occurred at the top of the seismic cloud, for which moment tensors could be computed. As we show below, the cluster of microearthquakes was migrating upward before the larger events were triggered as illustrated in the animations (available at <https://doi.org/10.5281/zenodo.13882152>).

Figure 10 shows the situation almost 2 hr later (49.5 hr after July 18, 00:00). In this short time, the plate boundary itself has been activated by a number of larger events between 2 and 4 km depth and by microearthquakes in the depth layer below. The b -value in this phase is lower, at around 1.0, indicating a shift in the earthquake size distribution (Figure S13 in Supporting Information S1). The highest event rates and the most recent events occur in a circular spreading front. In map view, the seismicity is now aligned along the p1 profile. The strike-slip solutions of the moment tensors agree very well with the elongated pattern of seismicity, indicating that shear stress is being released at the plate boundary. The projection of the moment tensor events in the vertical section orthogonal to p1 allows the dip angle and geometry of the plate boundary fault to be inferred. It is very likely that the moment tensor events ruptured EW planes and not NS-oriented en-echelon structures as is often assumed, for the larger earthquakes in the South Iceland seismic bookshelf transform zone to the east of the Hengill system. However, we will later discuss the largest M_w 5.6 earthquake, which may also have involved NS-oriented rupture planes.

In Figure 11, we finally project the seismicity onto vertical and horizontal cross-sections. Earthquakes occurring within a cube volume surrounding the projection axes are represented by colored circles; others are represented by open circles. Prior to 47 hr (July 18, 00:00), the swarm is concentrated at a depth of about 4.5–7 km and produces microearthquakes. At hour 47, an upward migration of microearthquakes begins with a mean velocity of the distribution of about 1.4 km/h (gray dashed line in Figure 11b). The earthquakes also become larger. Lateral growth starts at 47.7 hr with a propagation velocity between 10, km/h and 15, km/h (yellow-dashed line in

Figures 11a and 11b). Lateral growth in the brittle part of the plate boundary above 4 km depth is characterized by larger magnitude earthquakes. Comparable intrusions occurred later to the east, in some cases rupturing the brittle part of the plate boundary (e.g., days 239 and 242), and in others not (e.g., day 203). Examples are shown in Figures S11 and S14 in the Supporting Information S1.

Snapshots projected along the crossing profiles p2-p4 show that en-echelon structures have developed not only for shear fractures parallel to the plate boundary but also for intrusive fractures sub-parallel to the fissure swarms of the volcanic systems (see Figures S15, S16, and S17 in Supporting Information S1).

4.2. Centroid Moment Tensors

4.2.1. Reliability, Consistency, and Significance of Moment Tensor Solutions

A well-distributed network of high-quality seismic stations at regional and local distances is required to calculate well-constrained CMTs for small-magnitude earthquakes. The solutions are only reliable if both P- and S-waves, and preferably also surface waves, are used. The limitation of body-wave inversion is that one usually has to work in a frequency range above 0.5 Hz, which requires very well-tested and accurate velocity models. Inversions with dominant frequencies above 4 Hz are usually not reliable in our experience. Regional distance surface waves can be inverted at much lower frequencies, for example, between 0.04 and 0.2 Hz, which lessens the impact of inaccuracies in the velocity model, but requires wide- or broadband recordings and shallow earthquakes. Joint inversion of amplitude spectra and full waveforms is recommended. In addition to the second-order moment tensor, source studies should simultaneously invert for the centroid location and the centroid time. Otherwise, the interpretation of the *nonDC* components is questionable in particular, since third and higher-order terms in the moment tensor multiple expansion do not vanish and can be mapped into virtual *nonDC* components. It is also very important to sample the full model space to capture uncertainties and trade-offs of solutions. Finally, reliability and robustness testing with bootstrapping of input data and variation of velocity models is recommended. All these recommendations and conditions were taken into account in our case, making our study one of the most careful source mechanism studies on the RP. For instance, we were able to use 25 high-quality stations with good azimuthal coverage complemented by 40 virtual channels of DAS strain-rate recordings over a length of 21 km close to the epicentral area. We combined P- and S-wave amplitude spectra and full waveforms with Rayleigh and Love waves, P-wave arrival times, and first motion polarities in a joint inversion (Table 1). The centroid location and time are estimated in a probabilistic parameter search. The azimuthal coverage of the stations is exceptionally good, and the waveform fits are very convincing. The different data types can be fit very consistently so that we get very small error bounds.

Earthquake depths on the RP are usually shallow, with the BDT estimated at 6–7 km depth (Flóvenz et al., 2022). The hypocentral depths of the studied events is reported by IMO to be between 4 and 7 km. In contrast, the centroid depths are systematically shifted to shallower depths in the range of 0.6–5.0 km, mainly ranging from 2 to 5 km, with the median of the depth uncertainties being only 0.2 km (Figures 6d and 6e). The shallowest event, with a magnitude of M_w 3.7, occurred on 18 July 2020 at 5:54 UTC, just beneath the site of the future eruptions on the Sundhnúkar crater row in Svartsengi, expected in 2023 and 2024. The shallower depth can be explained by the much denser network of temporary stations we could use for the centroid location. Furthermore, the DAS cable runs almost across the epicentral region, imposing additional constraints on the depths of the earthquake. Earthquakes confined to a depth layer between the surface and 4 km indicate a hot crust and a shallow BDT, doming up to roughly 3–5 km depth beneath the geothermal fields on the RP (Flóvenz et al., 2022).

4.2.2. Robustness and Reliability of *nonDC* Components

The robustness and reliability of the components *nonDC* in general and the isotropic components, in particular, have been debated in previous studies (Dufumier & Rivera, 1997; Kühn et al., 2020; Zahradnik et al., 2008). Systematic errors such as inaccurate velocity models, the lack of near-surface information in the vicinity of the station, and inconsistent centroid locations can cause spurious *nonDC* components (Frohlich, 1994). Therefore, we performed different sensitivity analyzes to obtain the most accurate results. First of all, our method inverts for centroid location and moment tensor simultaneously using the same waveforms and filters, so that a bias from inconsistent centroid locations can be excluded. Additionally, we considered various different velocity models and concluded that *nonDC* components are stable and not affected by the choice of the velocity models. However, M_{cld} components show higher uncertainty up to by 13% than M_{iso} components. Hudson plots of the ensemble of

bootstrap solutions also confirms a systematic positive sign of isotropic components for single event, while M_{clvd} components scatter around zero (Figure 5). We also conducted tests of the effect of different frequency ranges on M_{clvd} and M_{iso} components and found almost no influence on the M_{iso} component. This indicates that the volumetric source component is generated instantaneously together with the shear rupture. Furthermore, errors due to stations and sensors can introduce systematic artifacts in the CMT results. Therefore, we carefully evaluated the quality of the data and tested that the arbitrary exclusion of different sensors and networks from the waveform inversion did not significantly change the existence of M_{iso} components.

In addition, from theoretical considerations, it can be expected that the inversion of amplitude spectra may generate artificial M_{iso} components if the ambient noise level is high. For instance, in Iceland, strong primary and secondary microseisms may be generated by oceanic waves in the Atlantic Ocean with dominant frequencies between 0.04 and 0.2 Hz (e.g., Dahm et al., 2006). Although we combine the amplitude spectra inversion with time-domain full waveforms, we want to exclude any possible influence from microseismic noise, especially for the surface waves. Therefore, we conducted a test in which only signals of microseisms were inverted with the same Bayesian method, using the same frequency band and window length for surface waves as in our earthquake study. Our results were conclusive: microseisms do not produce any significant M_{iso} components during inversion, as shown in Figure S9 of Supporting Information S1. After these investigations, we are confident that the positive isotropic component is not an artifact generated by noise or by the selection of data and sensors.

Previous studies show the existence of *nonDC* components in CMTs near volcanic areas. For instance, Dreger et al. (2000) observed significant volumetric expansion from moment tensors indicating a direct link between the seismicity and hydrothermal or magmatic processes in the Long Valley Caldera in 1997. Passarelli et al. (2018) found ~50% *nonDC* components corresponding to a fault opening at the Jailolo Volcano, Indonesia. Andinisari et al. (2021) showed that the microearthquakes in Kolumbo and Anydros in the Santorini-Amargos zone at the Hellenic volcanic arc have positive *nonDC* components, which are possibly indicative of volcanic activity. Saraó et al. (2010) revealed that the percentage of *nonDC* components of the swarm-earthquakes substantially increased before the 2001 CMT. Shuler and Ekström (2009) observed -30% M_{clvd} components at the Nyiragongo Volcano just after the eruption in 2002 suggesting the collapse of the roof of a shallow magma chamber.

Figure 5 presents the ensemble means of the M_{iso} component of 83 studied events. They are all above zero with a mean ratio between the moment of the isotropic and full moment tensor of $\approx 15\%$ indicating a volume expansion. \pm Isotropic in Figure 5 is defined by $\frac{tr}{|tr|} \frac{M_{iso}}{M_T}$, with $tr = (M_{11} + M_{22} + M_{33})/3$ and $M_T = \sqrt{M_{pq}^2 M_{pq}^2 / 2}$ and $M_{iso} = tr / \sqrt{6}$ (see e.g., Dahm & Krüger, 2014). The volume can be estimated by $\Delta V = tr / (\lambda + 2\mu/3)$ for a tensile crack and $\Delta V = tr / (\lambda + 2\mu)$ for an explosion source (Müller, 2001). Using Lamé's constants of $\lambda \approx \mu \approx 30 \text{ GPa}$ and events with a moment magnitude of $M_W = 3.5$ (20 July 2020) and $M_W \approx 4.5$ (19 July 2020), the co-seismic volume expansion is in the range of 800 m^3 and $26,000 \text{ m}^3$, respectively. For comparison, the estimated co-seismic volume expansion (ISO = 8%) accompanying an M_L 2.3 earthquake beneath Eyjafjallajökull volcano in June 1994 was 35 m^3 (Dahm & Brandsdóttir, 1997).

4.2.3. The Usage of DAS Data in Centroid Moment Tensor Inversion

At a first glance, first motion polarities extracted from the 21 km long dark fiber (DAS) are compatible with the results of the CMT inversion. We were therefore interested in investigating whether DAS data could be employed to further improve the quality of solutions. To this end, we analyzed which features of the DAS data may be used in seismic source studies. During the period of operation, most earthquakes ($M_W > 2.5$) occurred in the eastern part of the DAS cable and therefore, showed clear strain rate polarities along the cable. However, most of the virtual stations are unfortunately aligned on the nodal planes between the compressional and dilatational quadrants of the moment tensor and therefore show only emergent first motions.

In general, the DAS data was of lower quality and possessed a lower SNR. Other unknowns in the use of DAS data were the coupling to the ground, site conditions and the particular layout of the buried dark fiber cable. We recommend that these aspects are considered prior to any DAS cable installation, especially in a volcanic environment, in order to perform reliable seismic source studies (see also, Klaasen et al., 2021). If the DAS cable had been positioned more advantageously in relation to the nodal planes, waveforms recorded on the DAS could potentially be used as cross-correlation traces jointly with other types of waveforms in the CMT inversion, despite the instrument response not being known. On the other hand, the limitations are less severe for methods that use

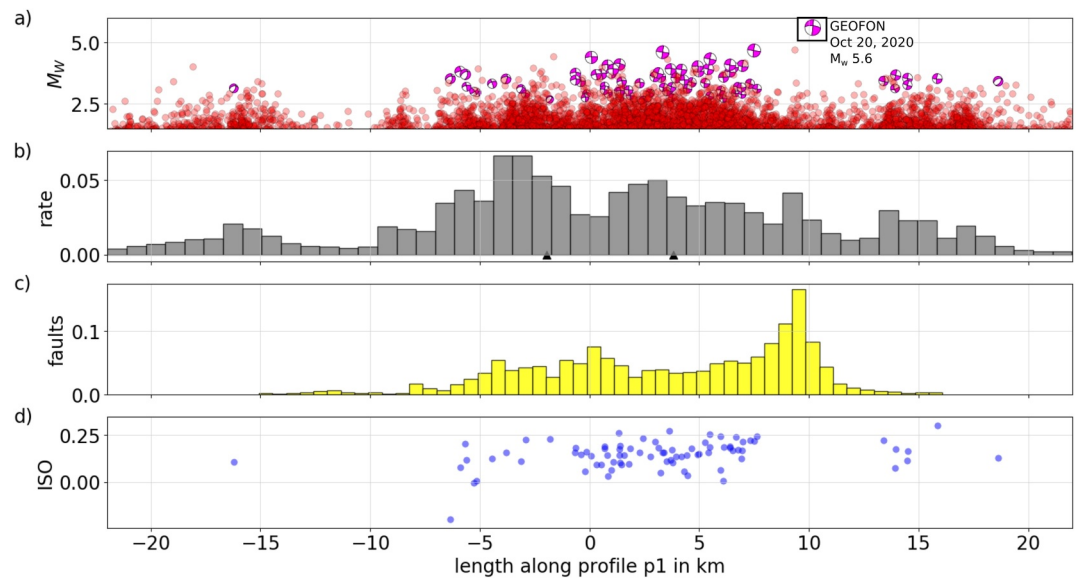


Figure 12. (a) Magnitude (M_W) and seismicity, (b) the earthquake rate, (c) the density of active surface faults and fractures from 2019 to 2020, and (d) the volumetric source component (M_{iso}) as a function of the length along profile p1. The magenta beach-balls in (a) represent events with high-quality CMT solutions. The black triangles in (b) indicate the crossing points of eruption fissures at Svartsengi (−5 km) and Fagradalsfjall (0 km). The surface fault data set was taken from Ducrocq et al. (2024).

travel time and azimuth information, for example, for event detection or location (Li & Zhan, 2018). Thus, we only included DAS-based P-wave first arrival times as an additional target group (Table 1) in the joint inversion and excluded polarities. Especially, the arrival times of the P-waves along the dense array of virtual sensors of the DAS provide additional constraints on the epicentral location and depth. In turn, a better understanding of the centroid location helps to further constrain the moment tensor parameters, and we could verify a further improvement in the fit and a reduction of uncertainties in the source parameters.

4.3. What CMTs and Swarms Tell About the Transtensional Opening Mechanisms?

Seismicity in 2020 is distributed in a 5 km wide zone along the oblique plate boundary on RP. Figure 12 shows the magnitude distribution, rate and isotropic components of events in our catalog along profile p1 (see Figure 7).

The earthquake rate and magnitudes in 2020 were high at and between the Svartsengi and Fagradalsfjall volcanic systems. The highest rates of microearthquakes correlate with locations where fissures occurred in 2021–2024 (Figure 12b). A third spot of high earthquake rate and large magnitudes is the Krýsuvík system, where no eruption has occurred so far.

The density of activated surface faults (Ducrocq et al., 2024) crossing p1 follows the general trend of higher magnitudes and seismic activity, and shows a peak at about 10 km where the largest earthquake (M_W 5.6) occurred (Figure 12c). Isotropic components (Figure 12d) do not correlate directly with specific eruption sites but are more generally linked to larger earthquakes triggered near the upper tip region of deep intrusions.

Flóvenz et al. (2022) pointed out the shallow micro seismicity occurring beneath Svartsengi related to the three uplift-subsidence cycles and the associated bending of the uppermost layers resulting from a pressure increase in a sill-shaped area at about 4 km depth. Geodetic observations of the uplift cycles also suggest sill-type intrusions beneath Svartsengi. Interestingly, the source region causing the uplift beneath Svartsengi did not show earthquakes below roughly 4 km depth, and the catalog of confined locations in this study indicates an up-doming of the deepest earthquakes beneath Svartsengi from about 7 to 4 km. The majority of the deeper seismicity and the largest events occurred east of Svartsengi, near the future eruption sites of Fagradalsfjall, and also close to Krýsuvík, 10 km east of Fagradalsfjall. According to Parks et al. (2023), these deep microearthquakes were possibly associated with mid-crustal magmatic intrusions at a depth of 6 km. Our analysis supports this model and

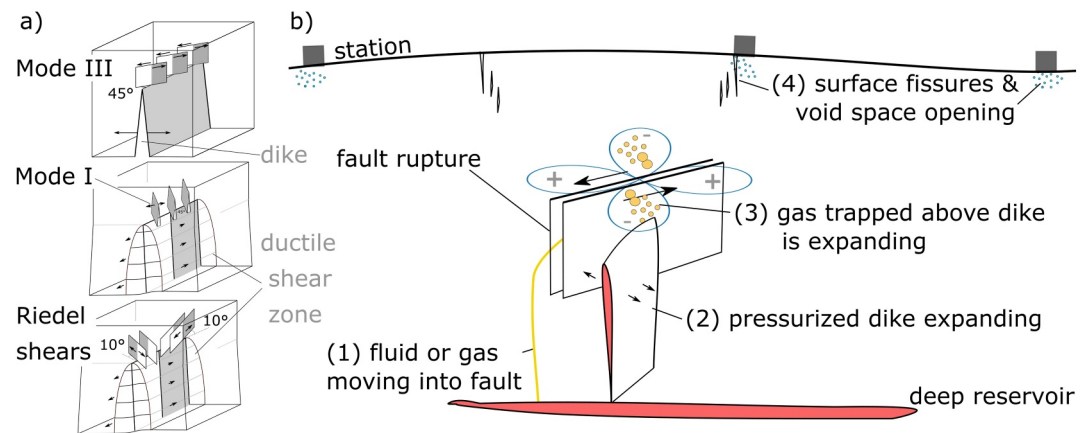


Figure 13. Sketch to demonstrate possible mechanisms for generating en-echelon faulting and diking and positive M_{1so} components. (a) Shear cracks can form in the border region of dikes or above ductile shear zones (Mode I, Mode III, Riedel shears). Opening cracks can form en-echelon structures above or below these ductile shear zones. (b) Four models explain co-seismic volume expansion. See the text for further explanation.

provides more details on where and how the intrusions were taking place and how they interact with the plate boundary.

The deeper seismicity beneath Fagradalsfjall is in a similar location as a group of long period earthquakes imaged at 10–12 km depth prior to and during the 2021 eruption, likely linked to the magma plumbing system beneath Fagradalsfjall (Greenfield et al., 2022). Our seismic catalog resolves that most deep intrusions in the beginning phase of the unrest occurred in vertical, en-echelon planes striking sub-parallel to the volcanic fissure swarms of the Reykjanes, Svartsengi, Fagradalsfjall, and Krýsuvík systems, perpendicular to the least compressive stress. The swarm-like seismicity in narrow bands with a width of only 1 km or smaller and the upward migration of the seismic front with velocities of only a few kilometer per hour suggest that these were ascending, buoyancy-driven magma-dikes, possibly accompanied by CO_2 degassing. Our study indicates that multiple, small-sized dikes ascended over a broader region of the plate boundary and formed distributed magmatic reservoirs in the lower and upper crust that were possibly depleted during later fissure eruptions.

The distribution of larger events is reflected in the 83 moment tensor solutions with $M_W > 2.7$ which align along a narrow, 30 km long segment centered on the 2021–2023 eruption sites at Fagradalsfjall and trending about $N80^\circ E$ (Figures 6 and 7). Interestingly, the CMT events occurred mainly at depths between 2 and 5 km, with the shallowest event at 0.6 km, and often sample the uppermost parts of the microearthquakes associated with intrusions. According to the well-resolved CMT inversions, most earthquakes occurred in the Fagradalsfjall segment, indicating NS -trending right-lateral or approximately $N80^\circ E$ trending left-lateral strike-slip faulting (Figure 6). This pre-dominance of strike-slip faulting in the transcurrent plate boundary zone is well known and has been explained by systems of sub-parallel, northerly striking right-lateral transcurrent faults that generate the largest earthquakes (Clifton & Kattenhorn, 2006; Einarsson, 1991; Einarsson et al., 2020, 2023). However, we cannot confirm northerly striking rupture planes for the events along the Fagradalsfjall segment but see indications of shear rupture along the plate boundary. We presented examples showing that the shear motion in the plate boundary was triggered by intrusions from depth. The formation of en-echelon structure, both from opening fractures by intrusions above or below a ductile shear zone, and from shear cracks associated with earthquakes above a ductile shear zone or above dikes (see Figure 13a), is well known from laboratory experiments in structural geology in the brittle layer above ductile shear zones.

The CMTs of the $M_W > 2.7$ earthquakes are predominantly strike-slip with positive isotropic components indicating co-seismic volume expansion. While the $\sim N80^\circ E$ striking nodal plane agrees surprisingly well with the spatial alignment and migration direction of microearthquakes in the upper crust, the co-seismic volume expansion needs further discussion. A simplest approach would be to interpret the increase in volume by shear-tensile crack in which the ratio of opening to shear is equal to the ratio of plate movement of 7 mm/yr versus 18 mm/yr = 0.38. However, the isotropic component of such a mixed mode rupture would be about 34%, about

twice the observed one. More critically, it would not be trivial to fill a compact fracture surface at a depth of 3–4 km with a frictional fluid in a few milliseconds if the fluid had to flow into the fault first.

Only a few mechanisms can be considered to explain a co-seismic volume expansion during the short duration of a shear rupture. Model (1) in Figure 13b depicts the aforementioned mixed-mode dislocation on the seismic fault at depth. Overpressure may be generated by an influx of magmatic fluids or gases from a deeper reservoir. The mixed-mode failure can be shown by a decomposition into a general dislocation source (Aki & Richards, 1980; Dahm, 1996; Vavryčuk, 2015), for which the magnitude of the positive M_{iso} component has a specific ratio to the moment of the *nonDC* component depending on the elastic properties of the media. Also, a positive M_{iso} should correlate with a positive M_{clvd} . Magma or water is ruled out as fluid because the flow velocity is too slow. However, if gas has previously intruded into the fault zone, then the co-seismic expansion of the gas in the shear fracture can proceed rapidly and open the fault surface during rupture.

Model (2) in Figure 13b assumes that a fluid-filled crack already exists close to the shear fault and possibly triggered the earthquake nearby. The fluid-filled crack may be a magmatic dike or sill under overpressure in its upper tip. As a response to shear failure in its vicinity, the dike will instantaneously expand and generate a co-seismic M_{iso} component. The dike expansion can be fast, even if magma-filled, because the fluids do not need to flow through narrow channels behind the rupture front, and only a small opening over the full surface of the dike is needed to explain a large M_{iso} . The model has been suggested by Dahm and Brandsdóttir (1997) to explain positive volumetric source components of microearthquakes beneath Eyjafjallajökull volcano at the eastern tip of the South Iceland Seismic Zone.

Models (3) and (4) in Figure 13b both display non-localized processes occurring remotely from the earthquake rupture. Based on the double-couple source assumption for a seismic source, which includes two quadrants—dilatant and compressional—that represent the areas of dilation and compression, Model (3) assumes a gas-saturated pore space in a dilatant quadrant for the rupture, where pore volume may expand when the rupture propagates. The gas may consist of CO_2 that migrated upward from the magmatic reservoirs in the lower crust and mantle and is trapped in the upper crust. The model predicts a positive M_{iso} component if the expansion of the pore gases outweighs the contraction of the pore space in other quadrants. A broad distribution of M_{clvd} components can be explained if the orientation of the fractures forming the pore space varies. Model (4) assumes that the volume expansion is generated near the surface. For instance, as the compressive pressure is small, opening cracks could appear with the arrival of seismic waves. This would be expected particularly if the uplift of the surface leads to tensile stresses. Model (4) is not very likely as a time delay can be expected between the seismic waves and the reaction of the aquifer close to the station.

Earthquakes in Iceland often display M_{iso} components due to volume changes, for instance in Krafla (Mildon et al., 2016; Schuler et al., 2016), at the Eyjafjallajökull volcano (Dahm & Brandsdóttir, 1997), and in Hengill (Miller et al., 1998). Foulger et al. (1989) observed microearthquakes in the Krafla area that had a variety of *nonDC* mechanisms, including explosive tensile-crack events and implosive events due to cavity collapse at depth. The existence of *nonDC* mechanisms on the RP was previously observed in the study of Hrubcová et al. (2021). They showed different signs of M_{iso} components associated with inflation (positive) and deflation (negative) during the swarm activity in 2017 related to a vertical magmatic dike.

Since in our study, most of the earthquakes have positive M_{iso} components with strike-slip mechanisms, confined to a very narrow zone both in time and space at a shallow depth, indicating a link between the magmatic system, vertical dikes, and earthquake activity, we infer that the M_{iso} component can be associated with a co-seismic widening of dikes and a possible volume increase of gas-saturated pore space close to the fault.

Returning to our key questions, how does the transtensional opening of the brittle part of a plate boundary work mechanically? Melt transfer in the lower crust occurs along the 70 km length of the plate boundary in the form of multiple, vertically extended, buoyancy-driven intrusions, with their horizontal axes oriented in the direction of the maximal compressive stress (σ_1), slowly ascending (< 2 km/hr) to the brittle-ductile transition of the plate boundary, and in some cases, at shallower depths. The intrusions are accompanied by tiny earthquake swarms with magnitudes smaller than about 2. At the depth of the brittle-ductile transition, we observe a strong interaction of dikes with the plate boundary fault, which is tilted about 30° with respect to σ_1 . Melt appears to infiltrate the fault from below, inducing shear in the fault that propagates laterally and upward at velocities of 10–15 km/hr. The slow slip events are accompanied by larger earthquakes, reaching magnitudes of five or greater. These events

indicate co-seismic volume expansion, which may result from the interaction of melt and fluids or gases in neighboring dikes and pore space. The complex interaction of multiple subparallel dikes with the plate boundary leads to the formation of fault systems that together create a wider deformation band accommodating tectonic stresses from surface aseismic faults and shallow microearthquakes.

5. Conclusions

This study enhances our understanding of seismogenic processes and their interplay with magmatic and tectonic activities on the Reykjanes Peninsula in Iceland. It elucidates how transtensional opening in the brittle part of a plate boundary is driven by the interaction between melt-induced dike intrusions and tectonic stresses. In oblique spreading zones like the Reykjanes Peninsula rift, this interaction leads to a complex system of faulting and deformation that accommodates both the ascent of magma and the lateral propagation of shear slip along the plate boundary. These mechanisms contribute to the development of broader deformation zones of sub-parallel fissures and earthquake faults where tectonic and magmatic activities are intricately linked at various depths, ultimately influencing both seismic, aseismic, and volcanic phenomena.

The 2020 unrest marked the beginning of a longer process which culminated so far in several eruptions from 2021 to 2024 at different sites along the obliquely rifting plate boundary of the Reykjanes Peninsula. We developed a catalog of microearthquakes from an automatic processing of waveform data from 2020 with a new method involving machine learning and waveform attribute stacking with an octal tree search for location. This high-resolution, high-quality catalog gives insights into the interaction of magmatic dikes with microearthquakes and shear ruptures. From this we see deep, swarm-like, precursory seismicity at sites of impending eruptions in the Svartsengi-Fagradalsfjall volcanic systems. In addition, our results indicate that the Krýsuvík volcanic system could be preparing for a possible future eruption already since 2020. While the plate boundary and deformation zone trend at depth in a N70°E-direction, obliquely to the spreading of N121°, the magmatic intrusions into the crust form systems of sub-parallel, en-echelon dikes approximately in the NE-SW direction. They induce earthquakes at shallow depths in the uppermost crust, which in turn generate en-echelon fault systems in the EW and possibly NS direction.

Centroid moment tensor inversion has become a basic tool to analyze earthquake sources and their possible *nonDC* components, while their errors are rarely reported. In our study a probabilistic moment tensor inversion method is used providing uncertainties by exploiting data from several dense networks. We found very consistent orientations of the strike-slip mechanism along the plate boundary, including positive, isotropic components (M_{iso}) with an average fraction of 15% of the total seismic moment, indicating a co-seismic volume expansion between about 800–26,000 m^3 .

The M_{iso} components are uncorrelated with the M_{clvd} components, implying that they cannot be explained by mixed-mode dislocation on a single plate boundary fault. We explain the isotropic component by an interaction between magmatic intrusions and the derived magmatic gases with shear fractures in the dike damage zone. Additionally, void space and fissure formation at the surface may contribute to M_{iso} components in regions affected by uplift-induced tensile stresses.

This study has also shown that DAS data can provide valuable input to determine the centroid location and the position of nodal planes on the focal sphere with high accuracy. However, the integrating of strain-rate amplitudes measured on DAS into the CMT inversion was problematic, even after careful data evaluation and sensitivity analysis, indicating that the installation of high-quality seismic sensors with good azimuthal coverage is important for moment tensor studies and cannot be substituted by DAS.

Data Availability Statement

The supporting information includes Figures S1–S17 and Table S1 in Supporting Information S1, which can be found in Supporting Information S1. Compiled waveforms for the CMT inversion can be found for target events in the GFZ data library <https://doi.org/10.5880/GFZ.2.1.2024.002>. The CMT results obtained in this study are available as interactive online reports via the link <https://data.pyrocko.org/publications/grond-reports/2020-ice-land-reykjanes>. Seismic data from the permanent national seismic network in Iceland are available in the open database Icelandic Meteorological Office (1992). Data from temporary stations operated by the Geophysical

Institute of the Academy of Sciences of the Czech Republic (Horalek, 2013) are under embargo until April 2026. However, data for 2013–2020 are scheduled to be released on 1 January 2025 via an EIDA node. Until then, they are available on request from Jana Doubravová. Seismological data from temporary GFZ stations analyzed during the current study are available in the GEOFON repository (Dahm et al., 2020). Fiber optic data are available at Jousset et al. (2020). For each profile, p1, p2, p3, p4, a GIF animation of the time-space evolution of the seismicity is available in the Zenodo repository (Büyükakpınar, Isken, Heimann, et al., 2024; <https://doi.org/10.5281/zenodo.13882152>).

Acknowledgments

We thank the editors and the reviewers for their constructive comments and suggestions that helped us to improve the article. P. B. is funded by the projects 407141557 (LO 2505/1-1) and 517982028 (BU 4346/1-1) of the Deutsche Forschungsgemeinschaft (DFG, German Research Foundation). J.A.L.C. was financed by Consejería de Universidad, Investigación e Innovación and by ERDF Andalusia Program 2021–2027 (project C. EXP.178. UGR23); and plan propio de investigación of University of Granada, programa de proyectos de investigación precompetitivos de jóvenes investigadores (project PPJIA2023.002). The maps are generated using the visualization packages pyGMT (Uieda et al., 2022), Python (<http://www.python.org>) and Matplotlib (<https://matplotlib.org/>). The probabilistic source inversion method is performed using the Grond framework (Heimann et al., 2018) under the Pyrocko environment (<https://pyrocko.org/>). The seismic catalog used in this study is produced with Qseek software: a data-driven framework for machine-learning earthquake detection, localization and characterization method (<https://pyrocko.github.io/qseek>). The seismic catalog is obtained from Icelandic Meteorological Office (1992) for comparison in Figure 6d and Figure S5 in Supporting Information S1. The elevation data in Figure 1 is taken from <http://viewfinderpanoramas.org/dem3.html>. Open Access funding enabled and organized by Projekt DEAL.

References

- Akbarbayram, K., Kıranşan, K., Varolgüneş, S., Büyükakpınar, P., Karasözen, E., & Bayık, Ç. (2022). Multidisciplinary analyses of the rupture characteristic of the June 14, 2020, Mw 5.9 Kaynarçınar (Karlöva, Bingöl) earthquake reveal N70E-striking active faults along the Yedisu seismic gap of the North Anatolian fault zone. *International Journal of Earth Sciences*, 112(2), 1–21. <https://doi.org/10.1007/s00531-022-02256-4>
- Aki, K., & Richards, P. G. (1980). *Quantitative seismology, theory and methods*. W.H. Freeman and Co.
- Alvizuri, C., Silwal, V., Krischer, L., & Tape, C. (2018). Estimation of full moment tensors, including uncertainties, for nuclear explosions, volcanic events, and earthquakes. *Journal of Geophysical Research: Solid Earth*, 123(6), 5099–5119. <https://doi.org/10.1029/2017JB015325>
- Andinisari, R., Konstantinou, K. I., & Ranjan, P. (2021). Moment tensor inversion of micro earthquakes along the Santorini-Amorgos zone: Tensile faulting and emerging volcanism in an extensional setting. *Journal of Volcanology and Geothermal Research*, 420, 107394. <https://doi.org/10.1016/j.jvolgeores.2021.107394>
- Árnadóttir, T., Geirsson, H., & Einarsson, P. (2004). Coseismic stress changes and crustal deformation on the Reykjanes Peninsula due to triggered earthquakes on 17 June 2000. *Journal of Geophysical Research*, 109(9). <https://doi.org/10.1029/2004JB003130>
- Björnsson, S., Einarsson, P., Tulinius, H., & Hjartardóttir, Á. R. (2020). Seismicity of the Reykjanes Peninsula 1971–1976. *Journal of Volcanology and Geothermal Research*, 391, 106369. <https://doi.org/10.1016/j.jvolgeores.2018.04.026>
- Büyükakpınar, P., Isken, M. P., Dahm, T., Olivar-Castaño, A., Doubravová, J., Ohrnberger, M., et al. (2024). The earthquake relocation analysis (2018–2024) using automatic waveform detection and machine learning techniques in the NW Bohemia/Vogtland region. In *Proceedings of the ESC2024 - 39th General Assembly of the European Seismological Commission*.
- Büyükakpınar, P., Isken, M. P., Heimann, S., Dahm, T., Kühn, D., Starke, J., et al. (2024). Understanding the seismic signature of transtensional opening in the Reykjanes Peninsula Rift Zone, SW Iceland [Dataset]. *Zenodo*. <https://doi.org/10.5281/zenodo.13882152>
- Cesca, S., Metz, M., Büyükakpınar, P., & Dahm, T. (2023). The energetic 2022 seismic unrest related to magma intrusion at the North Mid-Atlantic Ridge. *Geophysical Research Letters*, 50(13), e2023GL102782. <https://doi.org/10.1029/2023GL102782>
- Clifton, A. E., & Kattenhorn, S. A. (2006). Structural architecture of a highly oblique divergent plate boundary segment. *Tectonophysics*, 419(1–4), 27–40. <https://doi.org/10.1016/j.tecto.2006.03.016>
- Cubuk-Sabuncu, Y., Jónsdóttir, K., Caudron, C., Lecocq, T., Parks, M. M., Geirsson, H., & Mordret, A. (2021). Temporal seismic velocity changes during the 2020 rapid inflation at Mt. Thorbjörn-Svartsengi, Iceland, using seismic ambient noise. *Geophysical Research Letters*, 48(11), e2020GL092265. <https://doi.org/10.1029/2020GL092265>
- Dahm, T. (1996). Relative moment tensor inversion based on ray theory: Theory and synthetic tests. *Geophysical Journal International*, 124(1), 245–257. <https://doi.org/10.1111/j.1365-246X.1996.tb06368.x>
- Dahm, T. (2000). On the shape and velocity of fluid-filled fractures in the earth. *Geophysical Journal International*, 142(1), 181–192. <https://doi.org/10.1046/j.1365-246x.2000.00148.x>
- Dahm, T., & Brandsdóttir, B. (1997). Moment tensors of microearthquakes from the Eyjafjallajökull volcano in South Iceland. *Geophysical Journal International*, 130(1), 183–192. <https://doi.org/10.1111/j.1365-246X.1997.tb00997.x>
- Dahm, T., Heimann, S., Funke, S., Wendt, S., Rappsilber, I., Bindi, D., et al. (2018). Seismicity in the block mountains between Halle and Leipzig, Central Germany: Centroid moment tensors, ground motion simulation, and felt intensities of two m_l≈3 earthquakes in 2015 and 2017. *Journal of Seismology*, 22(2), 985–1003. <https://doi.org/10.1007/s10950-018-9746-9>
- Dahm, T., Jousset, P., Heimann, S., Milkereit, C., Hersir, G. P., & Magnússon, R. (2020). MAGIC - Seismic network MAGma in ICeland [Dataset]. *GFZ Data Services*. <https://doi.org/10.14470/4U7575229166>
- Dahm, T., & Krüger, F. (2014). Moment tensor inversion and moment tensor interpretation. In P. Bohrmann (Ed), *New Manual of Seismological Observatory Practice* (Vol. 2, no. (nmsop-2), pp. 1–37). Deutsches GeoForschungsZentrum GFZ. https://doi.org/10.2312/GFZ.NMSOP-2_IS_3.9
- Dahm, T., Kuehn, D., Cesca, S., Heimann, S., & Isken, M. P. (2024). Earthquake moment magnitudes from peak ground displacements and synthetic Green's functions. *Seismica*, 3(2). <https://doi.org/10.26443/seismica.v3i2.1205>
- Dahm, T., Tilmann, F., & Phipps-Morgan, J. (2006). Seismic broadband ocean bottom data and noise observed with free-fall stations: Experiences from long-term deployments in the north Atlantic and Tyrrhenian Sea. *Bulletin of the Seismological Society of America*, 96, 647–664. <https://doi.org/10.1785/0120040064>
- Dreger, D. S., Tkalčić, H., & Johnston, M. (2000). Dilational processes accompanying earthquakes in the long valley caldera. *Science*, 288(5463), 122–125. <https://doi.org/10.1126/science.288.5463.122>
- Ducrocq, C., Árnadóttir, T., Einarsson, P., Jónsson, S., Drouin, V., Geirsson, H., & Hjartardóttir, Á. R. (2024). Widespread fracture movements during a volcano-tectonic unrest: The Reykjanes Peninsula, Iceland, from 2019–2021 TerraSAR-X interferometry. *Bulletin of Volcanology*, 86(14), 1–14. <https://doi.org/10.1007/s00445-023-01699-0>
- Dufumier, H., & Rivera, L. (1997). On the resolution of the isotropic component in moment tensor inversion. *Geophysical Journal International*, 131(3), 595–606. <https://doi.org/10.1111/j.1365-246X.1997.tb06601.x>
- Einarsson, P. (1991). Earthquakes and present-day tectonism in Iceland. *Tectonophysics*, 189(1–4), 261–279. [https://doi.org/10.1016/0040-1951\(91\)90501-I](https://doi.org/10.1016/0040-1951(91)90501-I)
- Einarsson, P. (2008). Plate boundaries, rifts and transforms in Iceland. *Jökull Journal*, 58(1), 35–58. <https://doi.org/10.33799/jokull2008.58.035>
- Einarsson, P., Hjartardóttir, Á. R., Hreinsdóttir, S., & Imsland, P. (2020). The structure of seismogenic strike-slip faults in the eastern part of the Reykjanes Peninsula Oblique Rift, SW Iceland. *Journal of Volcanology and Geothermal Research*, 391, 106372. <https://doi.org/10.1016/j.jvolgeores.2018.04.029>

- Einarsson, P., & Brandsdóttir, B. (1980). Seismological evidence for lateral magma intrusion during the July 1978 deflation of the Krafla volcano in NE-Iceland. *Journal of Geophysics*, 160–165. <https://doi.org/10.2172/890964>
- Einarsson, P., Eyjólfsson, V., & Hjartardóttir, Á. R. (2023). Tectonic framework and fault structures in the Fagradalsfjall segment of the Reykjanes Peninsula Oblique Rift, Iceland. *Bulletin of Volcanology*, 85(9), 9. <https://doi.org/10.1007/s00445-022-01624-x>
- Fischer, T., Vlček, J., Hrubcová, P., Doubravová, J., Ágústsdóttir, Þ., & Guðnason, E. Á. (2023). Stress transfer between volcanic dyke and seismic activity accompanying the 2021 and 2022 Fagradalsfjall eruptions, Iceland. In *EGU General Assembly Conference Abstracts* (p. EGU-16208). <https://doi.org/10.5194/egusphere-egu23-16208>
- Flóvenz, O. G., Wang, R., Hersir, G. P., Dahm, T., Hainzl, S., Vassileva, M., et al. (2022). Cyclical geothermal unrest as a precursor to Iceland's 2021 Fagradalsfjall eruption. *Nature Geoscience*, 15(5), 397–404. <https://doi.org/10.1038/s41561-022-00930-5>
- Foulger, G., Long, R., Einarsson, P., & Björnsson, A. (1989). Implosive earthquakes at the active accretionary plate boundary in Iceland. *Nature*, 337(6208), 640–642. <https://doi.org/10.1038/337640a0>
- Frohlich, C. (1994). Earthquakes with Non—Double-Couple mechanisms. *Science*, 264(5160), 804–809. <https://doi.org/10.1126/science.264.5160.804>
- Greenfield, T., White, R. S., Winder, T., & Ágústsdóttir, T. (2020). Seismicity of the Askja and Bárðarbunga volcanic systems of Iceland, 2009–2015. *Journal of Volcanology and Geothermal Research*, 391, 106432. <https://doi.org/10.1016/j.jvolgeores.2018.08.010>
- Greenfield, T., Winder, T., Rawlinson, N., MacLennan, J., White, R. S., Ágústsdóttir, T., et al. (2022). Deep long period seismicity preceding and during the 2021 Fagradalsfjall eruption, Iceland. *Bulletin of Volcanology*, 84(12), 101. <https://doi.org/10.1007/s00445-022-01603-2>
- Heimann, S. (2011). *A robust method to estimate kinematic earthquake source parameters*. Dissertation. University of Hamburg. <http://ediss.sub.uni-hamburg.de/volltexte/2011/5357>
- Heimann, S., Isken, M., Kühn, D., Sudhaus, H., Steinberg, A., Daout, S., et al. (2018). Grond - a probabilistic earthquake source inversion framework. <https://doi.org/10.5880/GFZ.2.1.2018.003>
- Heimann, S., Kriegerowski, M., Isken, M., Cesca, S., Daout, S., Grigoli, F., et al. (2017). Pyrocko - An open-source seismology toolbox and library. *GFZ Data Services*. <https://doi.org/10.5880/GFZ.2.1.2017.001>
- Heimann, S., Vasyura-Bathke, H., Sudhaus, H., Isken, M. P., Kriegerowski, M., Steinberg, A., & Dahm, T. (2019). A Python framework for efficient use of pre-computed Green's functions in seismological and other physical forward and inverse source problems. *Solid Earth*, 10(6), 1921–1935. <https://doi.org/10.5194/se-10-1921-2019>
- Horalek, J. (2013). Reykjanet [Dataset]. *International Federation of Digital Seismograph Networks*. https://doi.org/10.7914/SN/7E_2013
- Hrubcová, P., Doubravová, J., & Vavříček, V. (2021). Non-double-couple earthquakes in 2017 swarm in Reykjanes Peninsula, SW Iceland: Sensitive indicator of volcano-tectonic movements at slow-spreading rift. *Earth and Planetary Science Letters*, 563, 116875. <https://doi.org/10.1016/j.epsl.2021.116875>
- Hudson, J. A., Pearce, R. G., & Rogers, R. M. (1989). Source type plot for inversion of the moment tensor. *Journal of Geophysical Research*, 94(B1), 765–774. <https://doi.org/10.1029/JB094iB01p00765>
- Icelandic Meteorological Office. (1992). Icelandic National Digital Seismograph Network [Dataset]. *International Federation of Digital Seismograph Networks*. <https://doi.org/10.7914/ZKJM-TJ71>
- Jamalreyhani, M., Pousse-Beltran, L., Büyükkakpınar, P., Cesca, S., Nissen, E., Ghods, A., et al. (2021). The 2019–2020 Khalili (Iran) earthquake sequence—Anthropogenic seismicity in the Zagros simply folded belt? *Journal of Geophysical Research: Solid Earth*, 126(12), e2021JB022797. <https://doi.org/10.1029/2021JB022797>
- Jenkins, J., (2024). Seismic imaging of the Reykjanes Peninsular, Iceland: Crustal-scale context of the ongoing Reykjanes eruptions [Dataset]. *Northern News*. Zenodo. 1–18. <https://doi.org/10.5281/zenodo.13235058>
- Jost, M., & Herrman, R. (1989). A students guide to and review of moment tensors. *Seismological Research Letters*, 60(2), 37–57. <https://doi.org/10.1785/gssrl.60.2.37>
- Jousset, P., Hersir, G. P., Krawczyk, C., Wollin, C., Lipus, M., Reinsch, T., et al. (2020). MAGIC (Magma Iceland) [Dataset]. *GFZ Data Services*. <https://doi.org/10.14470/0W7575244885>
- Keiding, M., Lund, B., & Árnadóttir, T. (2009). Earthquakes, stress, and strain along an obliquely divergent plate boundary: Reykjanes Peninsula, southwest Iceland. *Journal of Geophysical Research*, 114(9), 1–16. <https://doi.org/10.1029/2008JB006253>
- Klaassen, S., Paitz, P., Lindner, N., Dettmer, J., & Fichtner, A. (2021). Distributed acoustic sensing in volcano-glacial environments—Mount Meager, British Columbia. *Journal of Geophysical Research: Solid Earth*, 126(11), e2021JB022358. <https://doi.org/10.1029/2021JB022358>
- Klein, F. W., Einarsson, P., & Wyss, M. (1977). The Reykjanes Peninsula, Iceland, earthquake swarm of September 1972 and its tectonic significance. *Journal of Geophysical Research*, 82(5), 865–888. <https://doi.org/10.1029/jb082i005p00865>
- Kühn, D., & Dahm, T. (2008). Numerical modelling of dyke interaction and its influence on oceanic crust formation. *Tectonophysics*, 447(1), 53–65. (Plate movement and crustal processes in and around Iceland). <https://doi.org/10.1016/j.tecto.2006.09.018>
- Kühn, D., Heimann, S., Isken, M. P., Ruigrok, E., & Dost, B. (2020). Probabilistic moment tensor inversion for hydrocarbon-induced seismicity in the Groningen gas field, The Netherlands, Part 1: Testing. *Bulletin of the Seismological Society of America*, 110(5), 2095–2111. <https://doi.org/10.1785/0120200099>
- Li, Z., & Zhan, Z. (2018). Pushing the limit of earthquake detection with distributed acoustic sensing and template matching: A case study at the Brady geothermal field. *Geophysical Journal International*, 215(3), 1583–1593. <https://doi.org/10.1093/gji/ggy359>
- Mildon, Z. K., Pugh, D. J., Tarasewicz, J., White, R. S., & Brandsdóttir, B. (2016). Closing crack earthquakes within the Krafla caldera, North Iceland. *Geophysical Journal International*, 207(2), 1137–1141. <https://doi.org/10.1093/gji/ggw325>
- Miller, A. D., Julian, B. R., & Foulger, G. R. (1998). Three-dimensional seismic structure and moment tensors of non-double-couple earthquakes at the Hengill—Grensdalur volcanic complex, Iceland. *Geophysical Journal International*, 133(2), 309–325. <https://doi.org/10.1046/j.1365-246X.1998.00492.x>
- Müller, G. (2001). Volume change of seismic sources from moment tensors. *Bulletin of the Seismological Society of America*, 91(4), 880–884. <https://doi.org/10.1785/0120000261>
- Parks, M., Sigmundsson, F., Drouin, V., Hjartardóttir, Á. R., Geirsson, H., Hooper, A., et al. (2023). Deformation, seismicity, and monitoring response preceding and during the 2022 Fagradalsfjall eruption, Iceland. *Bulletin of Volcanology*, 85(10), 60. <https://doi.org/10.1007/s00445-023-01671-y>
- Passarelli, L., Heryandoko, N., Cesca, S., Rivalta, E., Rasmid, Rohadi, S., et al. (2018). Magmatic or not magmatic? The 2015–2016 seismic swarm at the Long-Dormant Jailolo Volcano, West Halmahera, Indonesia. *Frontiers of Earth Science*, 6(79). <https://doi.org/10.3389/feart.2018.00079>
- Pedersen, G. B. M., Belart, J. M. C., Óskarsson, B. V., Gudmundsson, M. T., Gies, N., Högnadóttir, T., et al. (2022). Volume, effusion rate, and lava transport during the 2021 Fagradalsfjall eruption: Results from near real-time photogrammetric monitoring. *Geophysical Research Letters*, 49(13), e2021GL097125. <https://doi.org/10.1029/2021GL097125>

- Rivalta, E., & Dahm, T. (2006). Acceleration of buoyancy-driven fractures and magmatic dikes beneath the free surface. *Geophysical Journal International*, 166(3), 1424–1439. <https://doi.org/10.1111/j.1365-246X.2006.02962.x>
- Rubin, D. B. (1981). The Bayesian Bootstrap. *Annals of Statistics*, 9(1), 130–134. <https://doi.org/10.1214/aos/1176345338>
- Sæmundsson, K., & Sigurgeirsson, M. (2013). Reykjaneskagi náttúruvá á Íslandi. eldgos og jarðskjálftar. *Viðlagatrygging Íslands/Háskólaútgáfan*, 379–401.
- Sæmundsson, K., Sigurgeirsson, M. Á., & Friðleifsson, G. Ó. (2020). Geology and structure of the Reykjanes volcanic system, Iceland. *Journal of Volcanology and Geothermal Research*, 391, 106501. <https://doi.org/10.1016/j.jvolgeores.2018.11.022>
- Saraó, A., Cocina, O., Privitera, E., & Panza, G. F. (2010). The dynamics of the 2001 Etna eruption as seen by full moment tensor analysis. *Geophysical Journal International*, 181(2), 951–965. <https://doi.org/10.1111/j.1365-246X.2010.04547.x>
- Schuler, J., Pugh, D. J., Hauksson, E., White, R. S., Stock, J. M., & Brandsdóttir, B. (2016). Focal mechanisms and size distribution of earthquakes beneath the Krafla central volcano, NE Iceland. *Journal of Geophysical Research: Solid Earth*, 121(7), 5152–5168. <https://doi.org/10.1002/2016JB013213>
- Shuler, A., & Ekström, G. (2009). Anomalous earthquakes associated with Nyiragongo Volcano: Observations and potential mechanisms. *Journal of Volcanology and Geothermal Research*, 181(3), 219–230. <https://doi.org/10.1016/j.jvolgeores.2009.01.011>
- Sigmundsson, F., Parks, M., Geirsson, H., Hooper, A., Drouin, V., Vogfjörð, K. S., et al. (2024). Fracturing and tectonic stress drive ultra-rapid magma flow into dikes. *Science*, 383(6688), 1228–1235. <https://doi.org/10.1126/science.adn2838>
- Sigmundsson, F., Parks, M., Hooper, A., Geirsson, H., Vogfjörð, K. S., Drouin, V., et al. (2022). Deformation and seismicity decline before the 2021 Fagradalsfjall eruption. *Nature*, 609, 523–528. <https://doi.org/10.1038/s41586-022-05083-4>
- Stefánsson, R., Bödvarsson, R., Slunga, R., Einarsson, P., Jakobsdóttir, S., Bungum, H., et al. (1993). Earthquake prediction research in the South Iceland seismic zone and the SIL project. *Bulletin of the Seismological Society of America*, 83(3), 696–716. <https://doi.org/10.1785/BSSA0830030696>
- Templeton, D. C., & Dreger, D. S. (2006). Non-double-couple earthquakes in the Long Valley volcanic region. *Bulletin of the Seismological Society of America*, 96(1), 69–79. <https://doi.org/10.1785/0120040206>
- Tryggvason, A., Rögnvaldsson, S. T., & Flóvenz, O. G. (2002). Three-dimensional imaging of the P- and S-wave velocity structure and earthquake locations beneath Southwest Iceland. *Geophysical Journal International*, 151(3), 848–866. <https://doi.org/10.1046/j.1365-246X.2002.01812.x>
- Uieda, L., Tian, D., Leong, W. J., Jones, M., Schlitzer, W., Grund, M., et al. (2022). PyGMT: A Python interface for the generic mapping tools. *Zenodo*. <https://doi.org/10.5281/zenodo.7481934>
- Vavryčuk, V. (2015). Moment tensor decompositions revisited. *Journal of Seismology*, 19(1), 231–252. <https://doi.org/10.1007/s10950-014-9463-y>
- Violay, M., Gibert, B., Mainprice, D., Evans, B., Dautria, J.-M., Azais, P., & Pezard, P. (2012). An experimental study of the brittle-ductile transition of basalt at oceanic crust pressure and temperature conditions. *Journal of Geophysical Research*, 117(B3). <https://doi.org/10.1029/2011JB008884>
- Wang, R. (1999). A simple orthonormalization method for stable and efficient computation of Green's functions. *Bulletin of the Seismological Society of America*, 89(3), 733–741. <https://doi.org/10.1785/bssa0890030733>
- Weir, N., White, R., Brandsdóttir, B., Einarsson, P., Shimamura, H., & Shiobara, H. (2001). Crustal structure of the northern Reykjanes Ridge and Reykjanes Peninsula, southwest Iceland. *Journal of Geophysical Research*, 106(B4), 6347–6368. <https://doi.org/10.1029/2000JB900358>
- Zahradnik, J., Jansky, J., & Plicka, V. (2008). Detailed waveform inversion for moment tensors of M ~ 4 events: Examples from the Corinth Gulf, Greece. *Bulletin of the Seismological Society of America*, 98(6), 2756–2771. <https://doi.org/10.1785/0120080124>